

Broadband measurement of Feibelman’s quantum surface response functions

Zeling Chen,^{1,*} Shu Yang,^{1,*} Zetao Xie,^{1,*} Jinbing Hu,^{1,2} Xudong Zhang,¹ Yipu Xia,¹
Yonggen Shen,³ Huirong Su,³ Maohai Xie,¹ Thomas Christensen,⁴ and Yi Yang^{1,†}

¹*Department of Physics and HK Institute of Quantum Science and Technology, The University of Hong Kong, Pokfulam, Hong Kong, China*

²*College of Optical-Electrical Information and Computer Engineering, University of Shanghai for Science and Technology, Shanghai 200093, China*

³*Genuine Optronics Limited, Shanghai, China*

⁴*Department of Electrical and Photonics Engineering, Technical University of Denmark, Kgs. Lyngby, Denmark*

The Feibelman d -parameter, a mesoscopic complement to the local bulk permittivity, describes quantum optical surface responses for interfaces, including nonlocality, spill-in and-out, and surface-enabled Landau damping. It has been incorporated into the macroscopic Maxwellian framework for convenient modeling and understanding of nanoscale electromagnetic phenomena, calling for the compilation of a d -parameter database for interfaces of interest in nano-optics. However, accurate first-principles calculations of d -parameters face computational challenges, whereas existing measurements of d -parameters are scarce and restricted to narrow spectral windows. We demonstrate a general broadband ellipsometric approach to measure d -parameters at a gold–air interface across the visible–ultraviolet regimes. Gold is found to spill-in and spill-out at different frequencies. We also observe gold’s Bennett mode, a surface-dipole resonance associated with a pole of the d -parameter, around 2.5 eV. Our measurements give rise to and are further validated by the passivity and Kramers–Kronig causality analysis of d -parameters. Our work advances the understanding of quantum surface response and may enable applications like enhanced electron field emission.

In classical electrodynamics, induced charges are assumed to be located at exactly the ionic interfaces. This assumption is valid at the macroscopic level but gradually fails in the microscopic limit. The deviation from the classical behavior is described by the Feibelman d -parameters (Fig. 1a) [1–3]:

$$d_{\perp}(\omega) = \frac{\int_{-\infty}^{\infty} z \rho(z) dz}{\int_{-\infty}^{\infty} \rho(z) dz}, \quad d_{\parallel}(\omega) = \frac{\int_{-\infty}^{\infty} z \partial_x J(z) dz}{\int_{-\infty}^{\infty} \partial_x J(z) dz}. \quad (1)$$

where d_{\perp} and d_{\parallel} equal the centroids of the induced charge $\rho(z)$ and the normal derivative of the tangential current $J(z)$, respectively, at a planar interface [4–8]. The d -parameters are complex, dispersive (i.e., frequency-dependent), and depend on the materials that make up the interface. Conceptually, the d -parameters enable a comprehensive mesoscopic treatment of the quantum response effects at interfaces, including nonlocality [9–15], electron spill-in/out [16–19], and surface-enabled Landau damping [20–23] before the onset of quantum tunneling [24–26] and size quantization [27, 28] at the atomic length scale. Since inception, the study on the d -parameters has been carried out for about half a century [29–40]. During which the representative early experimental explorations had been the hunting of the multipole plasmon mode (also known as the Bennett mode [41]) in particular in simple Jellium-like metals [42–46].

Recently, the d -parameters can be included in the standard macroscopic Maxwell equations by a simple modification of the associated boundary conditions as self-consistent field discontinuities [47, 48], enabling the analysis and modeling of nonclassical nanoscale (≥ 1 nm) electromagnetic phenomena [49–58] with standard computational tools. This utility and ease of implementation has been well-demonstrated by its adoption in state-of-the-art computational frameworks for nanophotonics, such as the boundary element method [59], quasi-normal modes [60, 61], transformational optics [62], and fluctuational electrodynamics [63]. Building on these ad-

vances, recent work has firmly established that quantum surface effects, as described by the d -parameters, can strongly modify light-matter interactions across a wide variety of nanophotonic settings [64–70]. Given this, it is essential to develop theoretical and experimental methods for obtaining the d -parameters of technologically relevant optical interfaces, analogously to those used in determining the bulk permittivity.

On the theoretical side, time-dependent density functional theory within the jellium approximation has been widely applied to calculate d -parameters of simple alkali-like metals [1, 3, 71–73]. However, the jellium treatment is inadequate for transition metals, and in particular, for the noble metals that are of key photonic and plasmonic importance, due to the non-negligible screening from lower-lying orbitals [64, 72, 74]. This, combined with the challenges in going beyond the jellium approximation in a well-controlled and computationally feasible way, calls for the development of experimental techniques to measure d -parameters directly.

Among the earliest experimental work toward this direction is the evidence of Bennett mode in silver obtained via the differential energy loss in low energy electron diffraction [75]. Meanwhile, the observation of substantial quantum corrections in small nanospheres embedded in matrices enabled the extraction of d -parameters close to the nonretarded resonant frequency [76]. Analogous ideas were extended to the retarded regime via gap-plasmon nanoresonators, enabled by a quasi-normal-mode perturbation analysis [47]. Similarly, it has been shown that d -parameters can be extracted from the measured dispersion of highly-confined gap plasmons [13]. More recently, DC-biased single nanoresonators led to the observation of spectral shift and linewidth modifications [77], implicitly demonstrating an electrical tunability of d -parameters. The spectral ranges of these earlier measurements are all well below the nonretarded surface plasmon frequency of materials, and their narrowband nature requires modifying the geometry of structures to scan across frequen-

cies. As a result, the experimental tabulation of d -parameters remains highly challenging, especially in frequency ranges not covered by the resonant features of specific geometries. This conundrum has thus hindered the observation of the widely-predicted Bennett mode [41, 42] in a wide range of materials of plasmonic and photonic prominence and the confirmation of essential response function properties of d -parameters, such as passivity and the Kramers–Kronig (KK) relations [37–39, 78].

Here, we demonstrate a general ellipsometric approach to measuring d -parameters in a broadband manner using a gold–air interface in the visible and ultraviolet regimes spanning 2–6 eV. We confirm the feasibility of the approach using the Sobol’ sensitivity analysis and Monte Carlo simulations. Our measurements discover a surface-dipole Bennett mode near 2.5 eV and demonstrate that gold can spill either -in or -out, relative to the interface, depending on frequency. Finally, the broadband nature of our measurements enables the unprecedented direct experimental evidence and analysis of the KK relations and passivity of d -parameters.

Ellipsometry is a well-established technique for characterizing the bulk permittivity from a difference of reflection coefficients at a planar interface [79]. The experimental observables are Ψ and Δ which give the amplitude contrast and phase difference between the p- and s-polarized reflection coefficients r_p and r_s via $\tan \Psi e^{i\Delta} = r_p/r_s$. For a single planar interface comprising material 1 above and material 2 below, a set of quantum Fresnel equations (see Supp. Sec. S1) for r_p and r_s can be expressed through the Feibelman d -parameters, which incorporate the leading-order deviation from classical response [1, 31, 33, 65, 80, 81] (Fig. 1b):

$$\begin{aligned} r_p &= \frac{\varepsilon_2 k_{z,1} - \varepsilon_1 k_{z,2} + (\varepsilon_2 - \varepsilon_1)(iq^2 d_{\perp} - ik_{z,1} k_{z,2} d_{\parallel})}{\varepsilon_2 k_{z,1} + \varepsilon_1 k_{z,2} - (\varepsilon_2 - \varepsilon_1)(iq^2 d_{\perp} + ik_{z,1} k_{z,2} d_{\parallel})}, \\ r_s &= \frac{k_{z,1} - k_{z,2} + (\varepsilon_2 - \varepsilon_1)ik_0^2 d_{\parallel}}{k_{z,1} + k_{z,2} - (\varepsilon_2 - \varepsilon_1)ik_0^2 d_{\parallel}}, \end{aligned} \quad (2)$$

where $k_0 \equiv \omega/c$, $k_j \equiv \sqrt{\varepsilon_j}k_0$ for $j \in \{1, 2\}$, $k_{z,j} \equiv \sqrt{k_j^2 - q^2}$, and q is the in-plane wavevector. Evidently, the classical Fresnel equations are restored when $d_{\perp} = d_{\parallel} = 0$.

Figure 1c and d show the measured Ψ and Δ in our experiment on a gold–air interface (Supp. Sec. S6). The template-stripped gold samples are of uniform Au(111) orientation (Supp. Sec. S5.A) with a surface roughness (rms) of 0.311 nm (Supp. Sec. S5.B). The gold layer is effectively bulk, considering its 100 nm thickness that substantially exceeds the skin depth in the measured frequency region. For frequencies $\hbar\omega \gtrsim 2$ eV, both Ψ and Δ exhibit rich variations, which suggest the possibility of using the quantum Fresnel equations [Eq. (2)] to measure d -parameters. In fact, this possibility was suggested speculatively in early discussions [36, 80, 82, 83], but was seen as impractically challenging at fixed incident angles due to the difficulty of accurately quantifying the relatively minor quantum correction contributions without resonant enhancement.

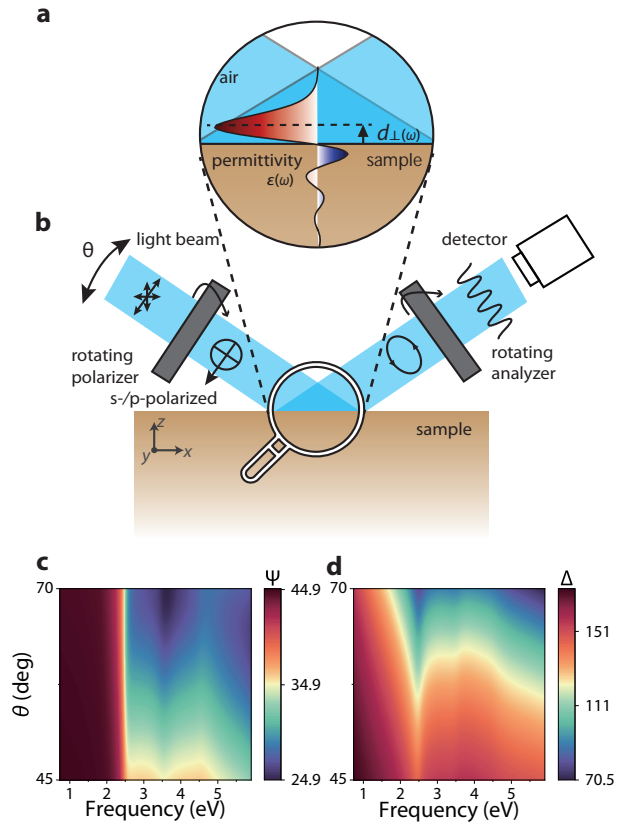


Figure 1. Experimental setup and measured amplitude contrast and phase difference. **a.** Conceptual schematic of induced charge density at an interface. d_{\perp} is the centroid of the induced charge. **b.** Ellipsometric setup. Incident light is linearly polarized under various incident angles θ , reflected by the surface, and detected to obtain the amplitude contrast $\Psi(\omega, \theta)$ and phase difference $\Delta(\omega, \theta)$. **c–d.** $\Psi(\omega, \theta)$ and $\Delta(\omega, \theta)$ of the gold–air interface averaged over all repeated measurements.

Using the gold–air interface as an example, we confirm the feasibility of ellipsometric determination of the d -parameters, using two independent methods, i.e., the Sobol’ sensitivity analysis and a Monte Carlo approach. In these methods (Fig. 2) and the data analysis below (Fig. 3), we assume $d_{\parallel} = 0$, which is generally expected at simple, charge-neutral interfaces [3, 31].

First, we apply the variance-based Sobol’ sensitivity analysis [84–86] to compare the relative weights of d_{\perp} and ε to observables and identify the frequency regimes where the ellipsometric method can apply. Intuitively, the Sobol’ analysis quantitatively attributes output variance to input variance (see Supp. Sec. S4.A for details). Of central importance is the total-effect index measuring the influence of an input, taking into account the interactions of that variable with all other inputs. Figure 2a–b shows the total-effect indices S_{μ}^{ν} , where $\mu = \{\text{Re } \varepsilon, \text{Im } \varepsilon, \text{Re } d_{\perp}, \text{Im } d_{\perp}\}$ and $\nu = \{\Psi, \Delta\}$, to characterize the total influence of the bulk permittivity and d_{\perp} -parameter under a range of incident angles and frequencies. Correspond-

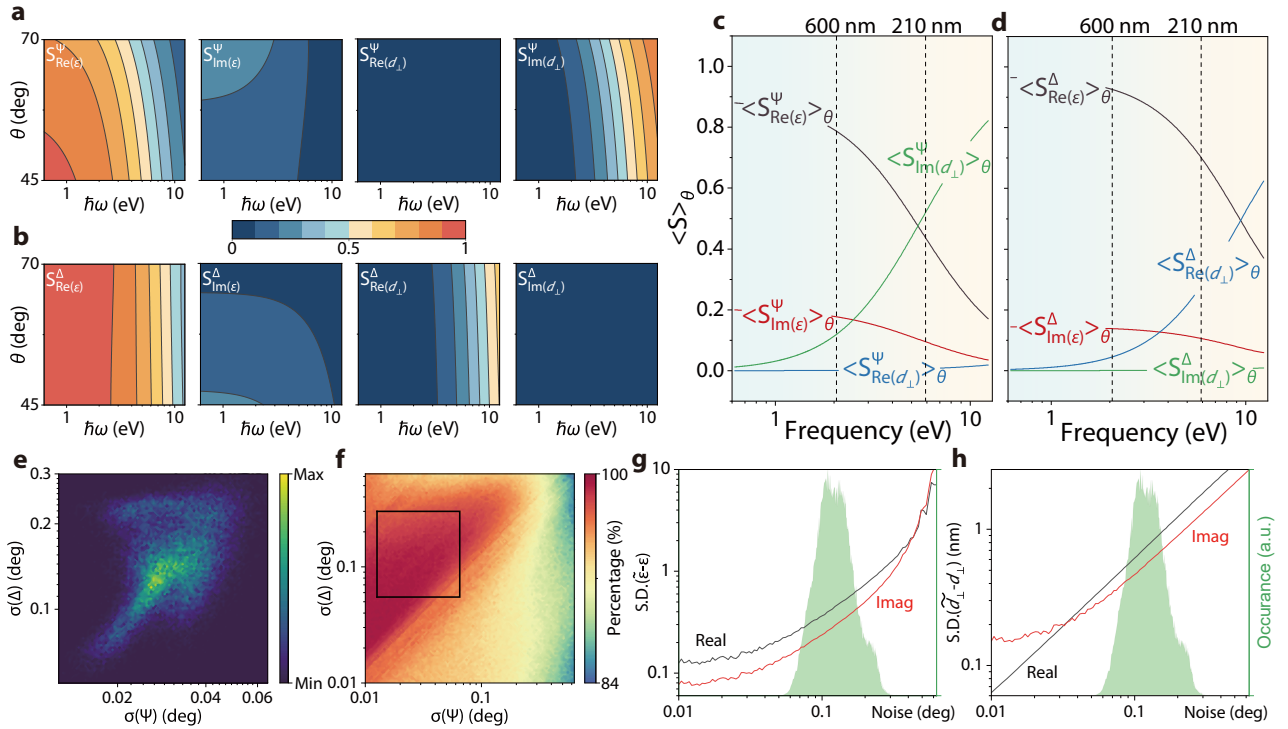


Figure 2. Measurement feasibility confirmed by Sobol' sensitivity analysis and Monte Carlo simulations. **a–b.** Total-effect indices $S_{\Psi, \Delta}^{\Psi, \Delta}$ describe the decomposed contributions from the bulk permittivity $\epsilon(\omega)$ and surface $d_{\perp}(\omega)$ to observables $\Psi(\theta, \omega)$ (a) and $\Delta(\theta, \omega)$ (b) at various incident angles. **c–d.** Angle-integrated total-effect indices $\langle S_{\Psi, \Delta}^{\Psi, \Delta} \rangle_{\theta}$. The gradient shading from blue to yellow indicates the increased and decreased contribution of $d_{\perp}(\omega)$ and $\epsilon(\omega)$, respectively, towards higher frequencies. The vertical dashed lines show the data analysis window, limited by the sensitivity of the d -parameter (low-frequency cutoff) and laser tunability (high-frequency cutoff). **e.** Experimental noise in ellipsometry observables Ψ and Δ . **f.** Percentage of Monte Carlo simulations where the ground truth of permittivity and d -parameter falls within the 3σ confidence interval (σ is the standard deviation) under various noise levels. The experimental noise statistics (e) lie within the black box in f. **g–h.** Standard deviations between fitting and ground-truth of ϵ (f) and d_{\perp} (g) of a single sampling. The histogram (shaded green in g–h) shows the experimental noise levels at various frequencies and incident angles.

ing angle-averaged indices are shown in Fig. 2c and d. In the Drude regime ($\hbar\omega \lesssim 2$ eV), the contributions from the bulk permittivity predominate the response of Ψ and Δ , complicating the extraction of d -parameters via ellipsometry. At higher frequencies ($\hbar\omega \gtrsim 2$ eV), however, the influence of ϵ and d_{\perp} become comparable, demonstrating the feasibility of ellipsometric d -parameter evaluation in this regime. A complementary sensitivity analysis (Supp. Sec. S4.B) confirms this conclusion. Notably, this regime covers a range above the screened plasma frequency where dielectric screening is non-negligible and where both theoretical and experimental results for d -parameters have thus far been lacking.

Second, we apply a Monte Carlo approach to confirm that the quantum Fresnel equations allow robust extraction of d_{\perp} also in the presence of experimental noise in Ψ and Δ (Fig 2e and green histograms in Fig. 2g–h). In the Monte Carlo simulation, we randomly choose the ground-truth combinations of ϵ and d_{\perp} , add noises of different levels to observables Ψ and Δ , and perform nonlinear least squares fitting to obtain estimates $\tilde{\epsilon}$ and \tilde{d}_{\perp} across a Monte Carlo ensemble (Supp. Sec.

S7.B). Within a 10^4 -ensemble dataset for each point in Fig. 2f and 10^6 -ensemble dataset in Fig. 2g–h, the ground truth falls within 3σ of the estimates with 99% likelihood (Fig. 2f). At an experimental (Ψ, Δ)-noise level of 0.1° (see the histogram in Fig. 2g–h), the single-sample standard deviations in ϵ is near 0.3 (Fig. 2g), while that of d_{\perp} is around 5 Å (Fig. 2h), both of which can be further reduced by repeated measurements.

Figure 3 shows the measurement data and associated analysis. We first compare the fitting residuals (Supp. Sec. S7.A) of the quantum Fresnel equations [Eq. (2)] with those of their classical counterpart in Fig. 3a. A substantial residual reduction, especially pronounced near 2.5 eV, is achieved with the quantum Fresnel equations, enabling us to simultaneously extract the bulk permittivity of gold (Fig. 3b) and the d_{\perp} of the gold–air interface (Fig. 3c). The thereby inferred bulk permittivity agrees well with the widely-used tabulated data from Palik [87] and from Johnson and Christy [88] (dotted and dashed lines in Fig. 3a). Moreover, the confidence intervals from the experimental fitting (shading in Fig. 3b–c) are also corroborated by post-measurement Monte Carlo analysis (Supp. Sec.

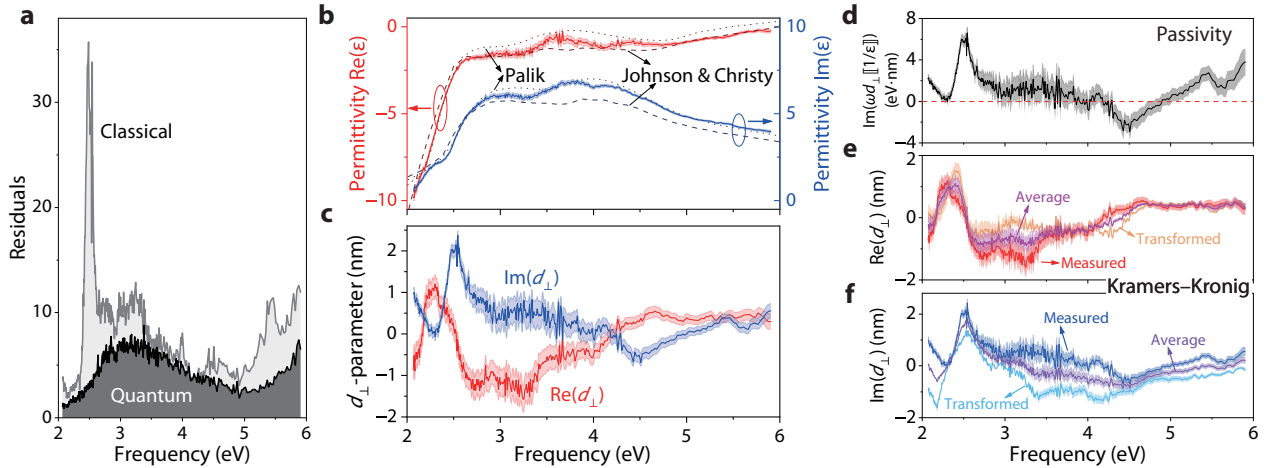


Figure 3. Measured d_{\perp} of the gold–air interface and its passivity and Kramers–Kronig analysis. **a.** The quantum Fresnel equations Eq. (2) reduces fitting residuals especially around 2.5 eV, suggesting a resonant behavior of $d_{\perp}(\omega)$. **b–c.** Measured bulk $\varepsilon(\omega)$ and surface $d_{\perp}(\omega)$. Real and imaginary parts are in red and blue, respectively, and shadings denote 3σ confidence interval derived from fitting. In b, dotted lines and dashed lines denote the Palik [87] and Johnson and Christy [88] data, respectively. In c, sharp variation of $d_{\perp}(\omega)$ appears near 2.5 eV in accordance with the residual reduction in a. **d.** The measured data satisfy the passivity requirement [Eq. (4a)] at most frequencies. **e–f.** The broadband measurement enables self-consistent Kramers–Kronig (KK) transformation between real (e) and imaginary (f) parts of $d_{\perp}(\omega)$, which includes the measured data, the KK-transformed data, and their average.

S7.C).

We emphasize two key features observed in the extracted $d_{\perp}(\omega)$ spectrum. First, in addition to the observation of charge spill-in ($\text{Re } d_{\perp} < 0$) at low frequencies ($\lesssim 2$ eV), in agreement with numerous earlier observations of nonclassical blueshifts in gold nanostructure spectra [47, 50, 53], we observe spill-out ($\text{Re } d_{\perp} > 0$) in the high-frequency tail. The onset of this spill-out regime is around 2.5 eV, slightly below the screened plasma frequency $\omega_p^* \approx 2.8$ eV. This observation of a high-frequency spill-out region in complement to a low-frequency spill-in region, is, in fact, a natural consequence and a first implicit experimental evidence of a KK-related sum rule [Eq.(5)], stating that $\int_0^{\infty} d\omega \text{Re } d_{\perp}(\omega) = 0$. Meanwhile, $\text{Im } d_{\perp}$ is non-negative, except for a narrow and likely spurious region near 4.5 eV.

Second, we discover a surface-dipole mode in gold, also known as the Bennett mode [41–43, 89, 90]. The mode is associated with the clear resonant peak feature [1, 71, 91] in $\text{Im } d_{\perp}(\omega)$ and an associated zero-crossing of $\text{Re } d_{\perp}(\omega)$ appears near 2.4–2.5 eV, i.e., with a pole of $d_{\perp}(\omega)$ at complex ω . The quality factor of the Bennett mode is measured as 13 from the width of $\text{Im } d_{\perp}$. Notably, this narrow spectral region is accompanied by a substantial residual reduction (Fig. 3a). The appearance of Bennett mode below the screened plasma frequency has been widely predicted theoretically [3, 64, 92, 93] and probed experimentally [42, 43, 45, 46, 75] in simple metals and silver, but its experimental confirmation has been lacking for gold thus far. We obtain consistent results in repeated time-separated measurements (Supp. Sec. S8.A) and across multiple samples (Supp. Sec. S8.B).

The measured d -parameters are several times larger than

previous calculations, which could reflect imperfections in earlier theoretical models and/or in our sample and measurement conditions; nevertheless, the magnitude of $\text{Re } d_{\perp}$ in our Au data is similar to that of Ag [76] near but below their screened plasma frequencies, respectively.

Additionally, by relaxing the assumption of $d_{\parallel} = 0$, we performed another type of fitting on the quantity $d_{\perp} - d_{\parallel}$ (See Refs. [1, 3, 33, 80] and Fig.S10 and Supp. Sec. S9) because (111) noble metals may host Shockley surface states that contribute to a nonzero d_{\parallel} [1, 92]. The extracted $d_{\perp} - d_{\parallel}$ is in quantitative agreement with $d_{\perp}(\omega)$ in Fig. 3c (which assumes $d_{\parallel}(\omega) = 0$), indicating the consistency and robustness of the data. The fine angular resolution in incident angles (Fig. 1c and d) generates a sufficiently large number of observations, which play a critical role in extracting the d -parameters with unprecedented accuracy in past inaccessible frequency regimes.

To carefully check the consistency of our extracted $d_{\perp}(\omega)$ values, we perform two additional validations: based, respectively, on requirements of passivity and causality. To this end, we first derive the constraints imposed by passivity by initially re-formulating the d -parameters via a nonclassical surface susceptibility (Supp. Sec. S3)

$$\chi(\mathbf{r}) = [d_{\perp} \llbracket 1/\varepsilon \rrbracket \hat{\mathbf{n}}\hat{\mathbf{n}}^T - d_{\parallel} \llbracket \varepsilon \rrbracket (\hat{\mathbf{I}} - \hat{\mathbf{n}}\hat{\mathbf{n}}^T)] \delta_{\partial\Omega}(\mathbf{r}), \quad (3)$$

which enables us to directly establish a passivity constraint by requiring that the influence of the d -parameters is strictly dissipative at all frequencies, i.e., that $\omega\chi$ be positive-definite

(Supp. Sec. S3)

$$\text{Im}(\omega d_{\perp}[\llbracket 1/\varepsilon \rrbracket]) \geq 0, \quad (4a)$$

$$\text{Im}(\omega d_{\parallel}[\llbracket \varepsilon \rrbracket]) \leq 0. \quad (4b)$$

Here, $\llbracket \mathbf{f} \rrbracket \equiv \mathbf{f}^+ - \mathbf{f}^-$ denotes the discontinuity of a scalar or vectorial field \mathbf{f} across an interface $\partial\Omega$ with outward normal $\hat{\mathbf{n}}$ and $\mathbf{f}^{\pm} \equiv (\mathbf{r}_{\partial\Omega} \pm 0^+ \hat{\mathbf{n}})$. $\delta_{\partial\Omega}(\mathbf{r})$ denotes a surface delta function associated with the interface $\partial\Omega$. The perpendicular and parallel component of \mathbf{f} is defined by $f_{\perp} \equiv \hat{\mathbf{n}} \cdot \mathbf{f}$ and $\mathbf{f}_{\parallel} \equiv (\hat{\mathbf{I}} - \hat{\mathbf{n}}\hat{\mathbf{n}}^T)\mathbf{f}$, $\hat{\mathbf{I}}$ is a unit-matrix and $\mathbf{r} \in \mathbb{R}^3$. In Eq. (4), the bulk permittivities across the interface are assumed isotropic.

We evaluate the passivity requirement using the ellipsoidally extracted $d_{\perp}(\omega)$ values in Fig. 3d. Except near the spurious region where $\text{Im} d_{\perp}(\omega) < 0$, around 4.5 eV, the passivity constraint is satisfied, also in accordance with our quantum surface energy dissipation calculation (See Supp. Sec. S11). The violation at 4.5 eV could e.g., be a result of the neglect of contributions from d_{\parallel} (see Fig. S10 and Supp. Sec. S9) or, considering the violation's modest magnitude and extent, as due to experimental imperfections. (See summary in Supp. Sec. S12)

Next, since the d -parameters must be causal functions, they are subject to a set of Kramers–Kronig (KK) relations (Supp. Sec. S2) [37, 78]

$$\text{Re} d_{\perp}(\omega) = \frac{2}{\pi} \int_0^{\infty} d\omega' \frac{\omega' \text{Im} d_{\perp}(\omega')}{\omega'^2 - \omega^2}, \quad (5a)$$

$$\text{Im} d_{\perp}(\omega) = -\frac{2}{\pi} \int_0^{\infty} d\omega' \frac{\omega \text{Re} d_{\perp}(\omega')}{\omega'^2 - \omega^2}. \quad (5b)$$

This KK relation was first obtained by Persson and Apell [78] decades ago but has remained experimentally elusive. The KK relations offer a path to validate the broadband consistency of extracted $d_{\perp}(\omega)$, by comparing the “bare” fit values to the corresponding values obtained by a subsequent KK transformation (with suitable low- and high-frequency extrapolation; see Supp. Sec. S10). To this end, we compare the directly extracted values of $d_{\perp}(\omega)$ to their KK-transformation, as well as their mutual average, in Fig. 3e–f. The key features of the spectra are consistent across these variants: in particular, the key resonant feature of the d -parameters at 2.4–2.5 eV are accordant.

Finally, we examine the implications of our measurement, particularly the Bennett mode, across three complementary scenarios, namely for the electron energy loss of a half-space (Fig. 4a) and a sphere (Fig. 4b), and field emission (Fig. 4c). First, we examine the energy loss of a single electron above a gold half-space in Fig. 4a (Supp. Sec. S13.C) [94]. The energy loss increases as the separation reduces in both classical and quantum calculations, whereas the latter exhibits stronger enhancement. More strikingly, at the small separation of $h = 1$ nm, a double-peak lineshape emerges where the high-frequency peak results from the excitation of surface plasmons as inherited from the classical treatment, whereas the new low-frequency peak is a direct consequence of the Bennett mode.

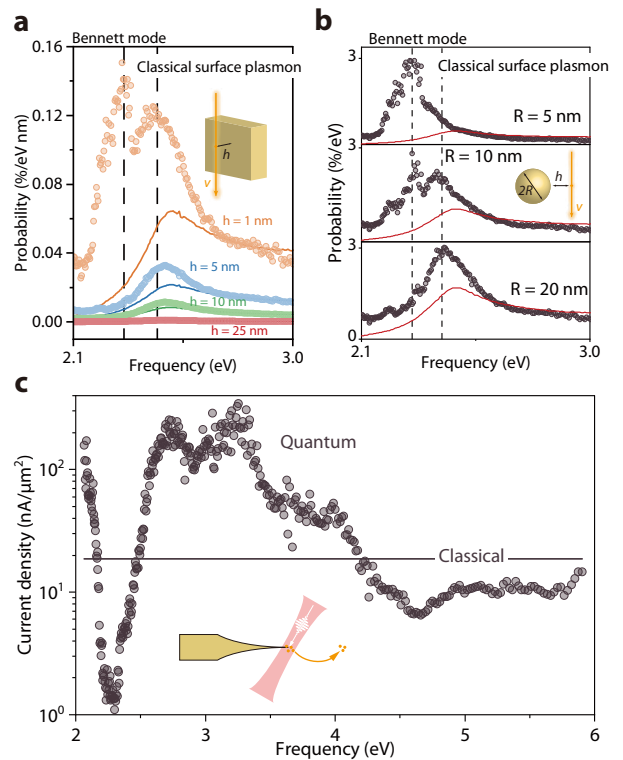


Figure 4. Quantum corrections and Bennett mode in electron energy loss and field emission. **a.** Enhancement of energy loss of a 10 keV electron moving parallel near a planar gold–air half-space at various separations. **b.** Enhancement of energy loss of a 10 keV electron moving near a gold sphere of different radii at separations of 1 nm. **c.** Enhancement and suppression of field emission under quantum correction. The peak field amplitude assumes $F_0 = 15$ V/nm, a repetition rate $f_R = 100$ MHz, and a full-width at half-maximum pulse duration of 10 fs. Solid lines and dots represent the classical and quantum-corrected results, respectively. The measured permittivity and d_{\perp} are both incorporated in the three calculations.

Second, we discuss the energy loss of a single electron near a gold sphere in Fig. 4b (Supp. Sec. S13.D) [94]. Surprisingly, with the sphere radius gradually decreasing, the dominant plasmonic modes shift from the classical surface plasmonic mode ($R = 20$ nm) to the Bennett mode ($R = 5$ nm). At the moderate radius $R = 10$ nm, two plasmonic modes share the equal weight, showing a double-peak lineshape in the spectrum.

Third, we investigate the quantum surface effects on field emission (Supp. Sec. S14), where the consequence of d -parameters has not been explored previously. The nonzero d_{\perp} contributes an out-of-plane surface dipole density of $\pi \equiv \varepsilon_0 d_{\perp}[\llbracket E_{\perp} \rrbracket] \hat{\mathbf{n}}$, which in turn shifts the work function by $\Delta\phi = -e\pi/\varepsilon_0$ [95, 96] due to surface charge redistribution induced by the field discontinuity in response to an ultrafast pulse (Fig. 4c inset). By inserting the field-modified work function in the Fowler–Nordheim equation, we obtain the changing of

current density due to the surface response shown in Fig 4c. The result predicts that it is possible to enhance or suppress the field emission by optically pumping a field emitter at a frequency where electrons spill-in or spill-out, respectively.

In conclusion, we demonstrate an ellipsometric approach for broadband measurement of the Feibelman d -parameters. The approach is verified and complemented by passivity and causality consistency tests. Gold is found to spill-in and -out in different frequency regimes and to exhibit a surface-dipole Bennett mode around 2.5 eV. Nevertheless, our measurement still has its limitations due to imperfections in surface adsorption, potential surface charging during sample peel-off, and surface roughness (see Supp. Sec. S12). These findings and limitations jointly call for future refined measurements at various interfaces, such as those consisting of metals with distinctly non-Drude dispersion, doped semiconductors [97], and even liquids [98], where the method demonstrated here can be generally applied. The methodology developed here can be adopted directly in commercial (and potential under vacuum conditions) ellipsometers and could inspire the development of tailored ellipsometric modulation and demodulation schemes [79] for community-wide access to d -parameter measurements and lead to their associated comprehensive cataloging. Such efforts would be useful in furthering the understanding of mesoscopic quantum effects in condensed matter physics, surface chemistry, vacuum electronics, and nanophotonics.

Acknowledgments. We thank Yuan Cao, Frankie Y. F. Chan, Sangyeon Cho, Yichen Feng, F. Javier García de Abajo, Francisco J. García-Vidal, James Hilfiker, Zemeng Lin, Tran Trung Luu, N. Asger Mortensen, Owen D. Miller, Tom Tiwald, and Ruichuan Zhang for experimental help and stimulating discussions.

* Z. C., S. Y., and Z. X. contributed equally to this work.

† yyig@hku.hk

- [1] P. J. Feibelman, *Progress in Surface Science* **12**, 287 (1982).
- [2] P. J. Feibelman, *Physical Review B* **12**, 1319 (1975).
- [3] A. Liebsch, *Electronic Excitations at Metal Surfaces* (Springer Science & Business Media, 2013).
- [4] N. A. Mortensen, *Nanophotonics* **10**, 2563 (2021).
- [5] C. Tserkezis, A. I. Fernández-Domínguez, P. A. D. Gonçalves, F. Todisco, J. D. Cox, K. Busch, N. Stenger, S. I. Bozhevolnyi, N. A. Mortensen, and C. Wolff, *Reports on Progress in Physics* **83**, 082401 (2020).
- [6] S. G. Menabde, J. T. Heiden, J. D. Cox, N. A. Mortensen, and M. S. Jang, *Nanophotonics* **11**, 2433 (2022).
- [7] F. Della Sala, *The Journal of Chemical Physics* **157**, 104101 (2022).
- [8] W. Yan and M. Qiu, *Nanophotonics* **11**, 1887 (2022).
- [9] A.D. Boardman, *Electromagnetic Surface Modes* (John Wiley & Sons, 1982).
- [10] A.I. Fernández-Domínguez, A. Wiener, F.J. García-Vidal, S.A. Maier, and J.B. Pendry, *Physical Review Letters* **108**, 106802 (2012).
- [11] S. Raza, S.I. Bozhevolnyi, M. Wubs, and N.A. Mortensen, *Journal of Physics: Condensed Matter* **27**, 183204 (2015).
- [12] P. A. D. Gonçalves, T. Christensen, N. M. Peres, A.-P. Jauho, I. Epstein, F. H. Koppens, M. Soljačić, and N. A. Mortensen, *Nature Communications* **12**, 3271 (2021).
- [13] S. Boroviks, Z.-H. Lin, V. A. Zenin, M. Ziegler, A. Dellith, P. A. D. Gonçalves, C. Wolff, S. I. Bozhevolnyi, J.-S. Huang, and N. A. Mortensen, *Nature Communications* **13**, 3105 (2022).
- [14] W. Ye, *Nano Letters* **23**, 7658 (2023).
- [15] I. Aupiais, R. Grasset, T. Guo, D. Daineka, J. Briatico, S. Houver, L. Perfetti, J.-P. Hugonin, J.-J. Greffet, and Y. Laplace, *Nature Communications* **14**, 7645 (2023).
- [16] E. J. Skjølstrup, T. Søndergaard, and T. G. Pedersen, *Physical Review B* **97**, 115429 (2018).
- [17] A. Campos, N. Troc, E. Cottancin, M. Pellarin, H.-C. Weissker, J. Lermé, M. Kociak, and M. Hillenkamp, *Nature Physics* **15**, 275 (2019).
- [18] G. Toscano, J. Straubel, A. Kwiatkowski, C. Rockstuhl, F. Evers, H. Xu, N. Asger Mortensen, and M. Wubs, *Nature Communications* **6**, 7132 (2015).
- [19] M. Khalid and C. Ciraci, *Communications Physics* **3**, 214 (2020).
- [20] C. Yannouleas and R. Broglia, *Annals of Physics* **217**, 105 (1992).
- [21] R. A. Molina, D. Weinmann, and R. A. Jalabert, *Physical Review B* **65**, 155427 (2002).
- [22] Z. Yuan and S. Gao, *Surface Science* **602**, 460 (2008).
- [23] J. Khurgin, W.-Y. Tsai, D. P. Tsai, and G. Sun, *ACS Photonics* **4**, 2871 (2017).
- [24] W. Zhu and K. B. Crozier, *Nature communications* **5**, 5228 (2014).
- [25] W. Zhu, R. Esteban, A. G. Borisov, J. J. Baumberg, P. Nordlander, H. J. Lezec, J. Aizpurua, and K. B. Crozier, *Nature Communications* **7**, 11495 (2016).
- [26] C. Deeb, J. Toudert, and J.-L. Pelouard, *Nanophotonics* **12**, 3029 (2023).
- [27] f. W. Halperin, *Reviews of Modern Physics* **58**, 533 (1986).
- [28] R. C. Monreal, T. J. Antosiewicz, and S. P. Apell, *New Journal of Physics* **15**, 083044 (2013).
- [29] A. Bagchi, *Physical Review B* **15**, 3060 (1977).
- [30] A. Brodsky and M. Urbakh, *Surface Science* **94**, 369 (1980).
- [31] P. Apell, *Physica Scripta* **24**, 795 (1981).
- [32] T. Maniv and H. Metiu, *Physical Review B* **22**, 4731 (1980).
- [33] W. Schaich and W. Chen, *Physical Review B* **39**, 10714 (1989).
- [34] R. Del Sole, *Solid State Communications* **37**, 537 (1981).
- [35] D. C. Langreth, *Physical Review B* **39**, 10020 (1989).
- [36] F. Abeles and T. Lopez-Rios, *Surface Science* **96**, 32 (1980).
- [37] B. Persson and E. Zaremba, *Physical Review B* **30**, 5669 (1984).
- [38] A. Liebsch, *Physical Review B* **32**, 6255 (1985).
- [39] K. Kempa and W. Schaich, *Physical Review B* **39**, 13139 (1989).
- [40] J. Tarriba and W. L. Mochan, *Physical Review B* **46**, 12902 (1992).
- [41] A. J. Bennett, *Physical Review B* **1**, 203 (1970).
- [42] K.-D. Tsuei, E. Plummer, A. Liebsch, K. Kempa, and P. Bakshi, *Physical Review Letters* **64**, 44 (1990).
- [43] K.-D. Tsuei, E. Plummer, A. Liebsch, E. Pehlke, K. Kempa, and P. Bakshi, *Surface Science* **247**, 302 (1991).
- [44] P. Sprunger, G. Watson, and E. Plummer, *Surface science* **269**, 551 (1992).
- [45] S. R. Barman, K. Horn, P. Häberle, H. Ishida, and A. Liebsch, *Physical Review B* **57**, 6662 (1998).
- [46] G. Chiarello, V. Formoso, A. Santaniello, E. Colavita, and L. Papagno, *Physical Review B* **62**, 12676 (2000).

- [47] Y. Yang, D. Zhu, W. Yan, A. Agarwal, M. Zheng, J. D. Joannopoulos, P. Lalanne, T. Christensen, K. K. Berggren, and M. Soljačić, *Nature* **576**, 248 (2019).
- [48] W. Yan, M. Wubs, and N. A. Mortensen, *Physical Review Letters* **115**, 137403 (2015).
- [49] U. Kreibitz and L. Genzel, *Surface Science* **156**, 678 (1985).
- [50] E. Cottancin, G. Celep, J. Lermé, M. Pellarin, J. Huntzinger, J. Vialle, and M. Broyer, *Theoretical Chemistry Accounts* **116**, 514 (2006).
- [51] S. Grammatikopoulos, S. Pappas, V. Dracopoulos, P. Pouloupoulos, P. Fumagalli, M. Velgakis, and C. Politis, *Journal of Nanoparticle Research* **15**, 1446 (2013).
- [52] S. Berciaud, L. Cognet, P. Tamarat, and B. Lounis, *Nano Letters* **5**, 515 (2005).
- [53] C. Ciraci, R. Hill, J. Mock, Y. Urzhumov, A. Fernández-Domínguez, S. Maier, J. Pendry, A. Chilkoti, and D. Smith, *Science* **337**, 1072 (2012).
- [54] J. A. Scholl, A. L. Koh, and J. A. Dionne, *Nature* **483**, 421 (2012).
- [55] S. Raza, N. Stenger, S. Kadkhodazadeh, S. V. Fischer, N. Koste-sha, A.-P. Jauho, A. Burrows, M. Wubs, and N. A. Mortensen, *Nanophotonics* **2**, 131 (2013).
- [56] D. Alcaraz Iranzo, S. Nanot, E. J. Dias, I. Epstein, C. Peng, D. K. Efetov, M. B. Lundberg, R. Parret, J. Osmond, J.-Y. Hong, *et al.*, *Science* **360**, 291 (2018).
- [57] H. Yang, X. Meng, S. Wu, J. I. Dadap, and R. M. Osgood, *Journal of the Optical Society of America B* **35**, 1442 (2018).
- [58] J. J. Baumberg, J. Aizpurua, M. H. Mikkelsen, and D. R. Smith, *Nature Materials* **18**, 668 (2019).
- [59] U. Hohenester and G. Unger, *Physical Review B* **105**, 075428 (2022).
- [60] C. Tao, Y. Zhong, and H. Liu, *Physical Review Letters* **129**, 197401 (2022).
- [61] Q. Zhou, P. Zhang, and X.-W. Chen, *Physical Review B* **105**, 125419 (2022).
- [62] F. Yang and K. Ding, *Physical Review B* **105**, L121410 (2022).
- [63] H. Zhang and K. Ding, arXiv preprint arXiv:2403.11849 (2024).
- [64] T. Christensen, W. Yan, A.-P. Jauho, M. Soljačić, and N. A. Mortensen, *Physical Review Letters* **118**, 157402 (2017).
- [65] P. A. D. Gonçalves, T. Christensen, N. Rivera, A.-P. Jauho, N. A. Mortensen, and M. Soljačić, *Nature Communications* **11**, 366 (2020).
- [66] C. Ciraci, R. Jurga, M. Khalid, and F. Della Sala, *Nanophotonics* **8**, 1821 (2019).
- [67] M. H. Eriksen, C. Tserkezis, N. A. Mortensen, and J. D. Cox, *Nanophotonics* (2024).
- [68] V. Karanikolas, I. Thanopoulos, J. D. Cox, T. Kuroda, J.-i. Inoue, N. A. Mortensen, E. Paspalakis, and C. Tserkezis, *Physical Review B* **104**, L201405 (2021).
- [69] A. Babaze, E. Ogando, P. E. Stamatopoulou, C. Tserkezis, N. A. Mortensen, J. Aizpurua, A. G. Borisov, and R. Esteban, *Optics Express* **30**, 21159 (2022).
- [70] A. Babaze, T. Neuman, R. Esteban, J. Aizpurua, and A. G. Borisov, *Nanophotonics* **12**, 3277 (2023).
- [71] A. Liebsch, *Physical Review B* **36**, 7378 (1987).
- [72] A. Liebsch, *Physical Review B* **48**, 11317 (1993).
- [73] N. Lang and W. Kohn, *Physical Review B* **1**, 4555 (1970).
- [74] P. J. Feibelman, *Physical Review Letters* **72**, 788 (1994).
- [75] F. Moresco, M. Rocca, V. Zielasek, T. Hildebrandt, and M. Henzler, *Physical Review B* **54**, R14333 (1996).
- [76] K.-P. Charlé, L. König, S. Nepijko, I. Rabin, and W. Schulze, *Crystal Research and Technology: Journal of Experimental and Industrial Crystallography* **33**, 1085 (1998).
- [77] L. Zurak, C. Wolf, J. Meier, R. Kulloock, N. A. Mortensen, B. Hecht, and T. Feichtner, *Science Advances* **10**, eadn5227 (2024).
- [78] B. Persson and P. Apell, *Physical Review B* **27**, 6058 (1983).
- [79] H. Fujiwara, *Spectroscopic Ellipsometry: Principles and Applications* (John Wiley & Sons, 2007).
- [80] K. Kempa and R. Gerhardt, *Surface Science* **150**, 157 (1985).
- [81] K. Kempa and W. Schaich, *Physical Review B* **34**, 547 (1986).
- [82] W. Schaich, *Physical Review B* **37**, 6193 (1988).
- [83] K. Kempa, *Surface Science Letters* **157**, L323 (1985).
- [84] I. M. Sobol', *Mathematics and Computers in Simulation* **55**, 271 (2001).
- [85] A. Saltelli, P. Annoni, I. Azzini, F. Campolongo, M. Ratto, and S. Tarantola, *Computer Physics Communications* **181**, 259 (2010).
- [86] J. Herman and W. Usher, *The Journal of Open Source Software* **2** (2017).
- [87] E. D. Palik, *Handbook of Optical Constants of Solids*, Vol. 3 (Academic press, 1998).
- [88] P. B. Johnson and R.-W. Christy, *Physical Review B* **6**, 4370 (1972).
- [89] H. M. Baghramyan, F. Della Sala, and C. Ciraci, *Physical Review X* **11**, 011049 (2021).
- [90] W. Yan, *Physical Review B* **91**, 115416 (2015).
- [91] K. Kempa and W. Schaich, *Physical Review B* **37**, 6711 (1988).
- [92] A. R. Echarri, P. A. D. Gonçalves, C. Tserkezis, F. J. García de Abajo, N. A. Mortensen, and J. D. Cox, *Optica* **8**, 710 (2021).
- [93] A. Liebsch and W. Schaich, *Physical Review B* **52**, 14219 (1995).
- [94] P. A. D. Gonçalves and F. J. García de Abajo, *Nano Letters* **23**, 4242 (2023).
- [95] T.-C. Leung, C. Kao, W. Su, Y. Feng, and C. T. Chan, *Physical Review B* **68**, 195408 (2003).
- [96] H. Ibach, *Physics of Surfaces and Interfaces*, Vol. 12 (Springer, 2006).
- [97] P. R. West, S. Ishii, G. V. Naik, N. K. Emani, V. M. Shalae, and A. Boltasseva, *Laser & Photonics Reviews* **4**, 795 (2010).
- [98] G. Lv, Y. Tu, J. H. Zhang, and G. Chen, *Proceedings of the National Academy of Sciences* **121**, e2320844121 (2024).

SUPPLEMENTARY INFORMATION

Broadband measurement of Feibelman's quantum surface response functions

Zeling Chen,^{1,*} Shu Yang,^{1,*} Zetao Xie,^{1,*} Jinbing Hu,^{1,2} Xudong Zhang,¹ Yipu Xia,¹ Yonggen Shen,³ Huirong Su,³ Maohai Xie,¹ Thomas Christensen,⁴ and Yi Yang^{1,†}

¹Department of Physics and HK Institute of Quantum Science and Technology, The University of Hong Kong, Pokfulam, Hong Kong, China

²College of Optical-Electrical Information and Computer Engineering, University of Shanghai for Science and Technology, Shanghai 200093, China

³Genuine Optronics Limited, Shanghai, China

⁴Department of Electrical and Photonics Engineering, Technical University of Denmark, Kgs. Lyngby, Denmark

CONTENTS

S1. The quantum Fresnel equations	1	S9. Alternative fitting on $d_{\perp} - d_{\parallel}$	11
S2. Kramers–Kronig relation and sum rules	2	S10. Kramers–Kronig extrapolation	13
S3. Passivity constraints for d -parameters	3	S11. Energy dissipation due to the surface dipole	13
S4. Model sensitivity analysis	4	S12. Measurement limitation	15
S5. Sample characterizations	5	S13. Quantum corrections to LDOS and EELS	15
S6. Ellipsometric measurements	7	S14. Quantum corrections to field emission	17
S7. Fitting methodology	7	References	18
S8. Temporal and cross-sample consistency	11		

S1. THE QUANTUM FRESNEL EQUATIONS

Here we derive Fresnel equations with quantum surface corrections. We first rewrite the mesoscopic boundary condition where d -parameters mediate self-consistent field discontinuities [S1].

$$[[D_{\perp}]] = -i\omega^{-1}\nabla_{\parallel} \cdot \mathbf{K} = d_{\parallel}\nabla_{\parallel} \cdot [[\mathbf{D}_{\parallel}]], \quad (\text{S1a})$$

$$[[B_{\perp}]] = 0, \quad (\text{S1b})$$

$$[[\mathbf{E}_{\parallel}]] = -\varepsilon_0^{-1}\nabla_{\parallel}\pi = -d_{\perp}\nabla_{\parallel}[[E_{\perp}]], \quad (\text{S1c})$$

$$[[\mathbf{H}_{\parallel}]] = \mathbf{K} \times \hat{\mathbf{n}} = i\omega d_{\parallel}[[\mathbf{D}_{\parallel}]] \times \hat{\mathbf{n}}. \quad (\text{S1d})$$

Here, $[[\mathbf{f}]] \equiv \mathbf{f}^+ - \mathbf{f}^-$ denotes the discontinuity of a field \mathbf{f} (an electric \mathbf{E} , displacement \mathbf{D} , magnetic \mathbf{B} or magnetizing \mathbf{H} field with determined frequency ω) across an interface $\partial\Omega$ with outward normal $\hat{\mathbf{n}}$. $\delta_{\partial\Omega}(\mathbf{r})$ denotes a surface delta function associated with the interface $\partial\Omega$. The field \mathbf{f}^+ and \mathbf{f}^- are defined as $\mathbf{f}^{\pm} \equiv (\mathbf{r}_{\partial\Omega} \pm 0^+ \hat{\mathbf{n}})$. The perpendicular and parallel component of the fields \mathbf{f} is defined by $f_{\perp} \equiv \hat{\mathbf{n}} \cdot \mathbf{f}$ and $\mathbf{f}_{\parallel} \equiv (\hat{\mathbf{I}} - \hat{\mathbf{n}}\hat{\mathbf{n}}^T)\mathbf{f}$, $\hat{\mathbf{I}}$ is a unit-matrix and $\mathbf{r} \in \mathbb{R}^3$. With these boundary conditions, we rederive the reflection and transmission coefficients of a planar interface. We adopt the same coordinate system as in Main Text Figure 1, i.e., material 1 at the top and material 2 at the bottom.

A. p-polarized waves

First, we focus on the transverse magnetic solutions:

$$\mathbf{H}_1 = \left(e^{-ik_{z,1}z} + r_p^{(H)} e^{ik_{z,1}z} \right) e^{i(qx - \omega t)} \hat{\mathbf{y}}, \quad (\text{S2a})$$

$$\mathbf{E}_1 = [E_{x,1}(z)\hat{\mathbf{x}} + E_{z,1}(z)\hat{\mathbf{z}}] e^{i(qx - \omega t)}, \quad (\text{S2b})$$

in the half-space of the material 1 ($z > 0$), and

$$\mathbf{H}_2 = t_p^{(H)} e^{-ik_{z,2}z} e^{i(qx - \omega t)} \hat{\mathbf{y}}, \quad (\text{S3a})$$

$$\mathbf{E}_2 = [E_{x,2}(z)\hat{\mathbf{x}} + E_{z,2}(z)\hat{\mathbf{z}}] e^{i(qx - \omega t)}, \quad (\text{S3b})$$

in the half-space of the material 2 ($z < 0$). q is the in-plane wavevector and $k_j \equiv \sqrt{\varepsilon_j}k_0$ for $j \in \{1, 2\}$ are the out-of-plane wavevectors. Here, the superscript “(H)” stands for magnetic fields. Using Maxwell’s equations, the amplitudes of the electric fields can be obtained as

$$E_{x,1}(z) = \frac{-k_{z,1}}{\omega\varepsilon_0\varepsilon_1} \left(e^{-ik_{z,1}z} - r_p^{(H)} e^{ik_{z,1}z} \right), \quad (\text{S4a})$$

$$E_{z,1}(z) = \frac{-q}{\omega\varepsilon_0\varepsilon_1} \left(e^{-ik_{z,1}z} + r_p^{(H)} e^{ik_{z,1}z} \right), \quad (\text{S4b})$$

$$E_{x,2}(z) = \frac{-t_p^{(H)}k_{z,2}}{\omega\varepsilon_0\varepsilon_2} e^{-ik_{z,2}z}, \quad (\text{S4c})$$

$$E_{z,2}(z) = \frac{-t_p^{(H)}q}{\omega\varepsilon_0\varepsilon_2} e^{-ik_{z,2}z}. \quad (\text{S4d})$$

At the planar interface, substituting Eqs. (S4) into the boundary conditions in Eqs. (S1), we get

$$\frac{k_{z,1}}{\varepsilon_1} (r_p^{(H)} - 1) + \frac{k_{z,2}}{\varepsilon_2} t_p^{(H)} = iq^2 d_\perp \left[\frac{1}{\varepsilon_1} (1 + r_p^{(H)}) - \frac{1}{\varepsilon_2} t_p^{(H)} \right], \quad (\text{S5a})$$

$$1 + r_p^{(H)} - t_p^{(H)} = -id_\parallel [k_{z,1} (r_p^{(H)} - 1) + k_{z,2} t_p^{(H)}]. \quad (\text{S5b})$$

With some algebraic derivations, one can obtain the quantum reflection and transmission coefficient for p-polarized wave, and translate in terms of electric fields with $r_p \equiv r_p^{(H)}$ and $t_p \equiv \sqrt{\frac{\varepsilon_1}{\varepsilon_2}} t_p^{(H)}$:

$$r_p = \frac{\varepsilon_2 k_{z,1} - \varepsilon_1 k_{z,2} + (\varepsilon_2 - \varepsilon_1) (iq^2 d_\perp - ik_{z,1} k_{z,2} d_\parallel) + (\varepsilon_2 k_{z,2} - \varepsilon_1 k_{z,1}) q^2 d_\perp d_\parallel}{\varepsilon_2 k_{z,1} + \varepsilon_1 k_{z,2} - (\varepsilon_2 - \varepsilon_1) (iq^2 d_\perp + ik_{z,1} k_{z,2} d_\parallel) - (\varepsilon_2 k_{z,2} + \varepsilon_1 k_{z,1}) q^2 d_\perp d_\parallel}, \quad (\text{S6a})$$

$$t_p = \sqrt{\frac{\varepsilon_1}{\varepsilon_2}} \frac{1}{1 - ik_{z,2} d_\parallel} \left[(1 + ik_{z,1} d_\parallel) r_p - ik_{z,1} d_\parallel + 1 \right]. \quad (\text{S6b})$$

If we only keep the leading linear order of $kd_{\perp,\parallel}$, the expressions reduce to

$$r_p = \frac{\varepsilon_2 k_{z,1} - \varepsilon_1 k_{z,2} + (\varepsilon_2 - \varepsilon_1) (iq^2 d_\perp - ik_{z,1} k_{z,2} d_\parallel)}{\varepsilon_2 k_{z,1} + \varepsilon_1 k_{z,2} - (\varepsilon_2 - \varepsilon_1) (iq^2 d_\perp + ik_{z,1} k_{z,2} d_\parallel)}, \quad (\text{S7a})$$

$$t_p = \frac{2\sqrt{\varepsilon_1 \varepsilon_2} k_{z,1}}{\varepsilon_2 k_{z,1} + \varepsilon_1 k_{z,2} - (\varepsilon_2 - \varepsilon_1) (iq^2 d_\perp + ik_{z,1} k_{z,2} d_\parallel)}. \quad (\text{S7b})$$

B. s-polarized waves

The derivation of quantum Fresnel reflection and transmission coefficients of s-polarized waves is similar to that of the p-polarized wave. The coefficients can be defined for the transverse electric fields. By applying the nonclassical boundary conditions, we get:

$$r_s = \frac{k_{z,1} - k_{z,2} + (\varepsilon_2 - \varepsilon_1) ik_0^2 d_\parallel}{k_{z,1} + k_{z,2} - (\varepsilon_2 - \varepsilon_1) ik_0^2 d_\parallel}, \quad (\text{S8a})$$

$$t_s = \frac{2k_{z,1}}{k_{z,1} + k_{z,2} - (\varepsilon_2 - \varepsilon_1) ik_0^2 d_\parallel}. \quad (\text{S8b})$$

S2. KRAMERS–KRONIG RELATION AND SUM RULES

As response functions, d_\perp naturally satisfy a set of Kramers–Kronig (KK) relations [S2]:

$$\text{Re} [d_\perp(\omega)] = \frac{2}{\pi} \int_0^\infty d\omega' \frac{\omega' \text{Im} [d_\perp(\omega')]}{\omega'^2 - \omega^2}, \quad (\text{S9a})$$

$$\text{Im} [d_\perp(\omega)] = -\frac{2}{\pi} \int_0^\infty d\omega' \frac{\omega' \text{Re} [d_\perp(\omega')]}{\omega'^2 - \omega^2}. \quad (\text{S9b})$$

Obtaining sum rules for d_{\perp} then follows directly from the KK relations [S2]. For $\text{Re}(d_{\perp})$, multiplying ω to Eq. (S9b) and taking the limit of $\omega \rightarrow \infty$, we have

$$\int_0^{\infty} d\omega \text{Re} [d_{\perp}(\omega)] = \frac{\pi}{2} \lim_{\omega \rightarrow \infty} \omega \text{Im} d_{\perp}(\omega). \quad (\text{S10a})$$

Using the asymptotic property that $d_{\perp}(\omega) \sim \omega^{-2}$ when $\omega \rightarrow \infty$ [S2], we can simplify the sum rule of $\text{Re} d_{\perp}$ in Eq. (S10a) to

$$\int_0^{\infty} d\omega \text{Re} [d_{\perp}(\omega)] = 0. \quad (\text{S11})$$

For $\text{Im}(d_{\perp})$, applying Eq. (S9a) at zero frequency produces

$$\int_0^{\infty} d\omega \frac{\text{Im} [d_{\perp}(\omega)]}{\omega} = \frac{\pi}{2} d_{\perp}(0). \quad (\text{S12})$$

S3. PASSIVITY CONSTRAINTS FOR d -PARAMETERS

The nonclassical surface dipole and current density can be recast through the introduction of a nonclassical surface susceptibility, thereby enabling the imposition of passivity constraints on the d -parameters. From Eqs. (S1c) and (S1a), the surface dipole $\boldsymbol{\pi}$ and current \mathbf{K} can be expressed as [S1]

$$\boldsymbol{\pi}(\mathbf{r}_{\partial\Omega}) \equiv \varepsilon_0 d_{\perp} \hat{\mathbf{n}} \hat{\mathbf{n}}^T \llbracket \mathbf{E} \rrbracket, \quad (\text{S13a})$$

$$\mathbf{K}(\mathbf{r}_{\partial\Omega}) \equiv i\omega d_{\parallel} (\hat{\mathbf{I}} - \hat{\mathbf{n}} \hat{\mathbf{n}}^T) \llbracket \mathbf{D} \rrbracket. \quad (\text{S13b})$$

The induced current is equivalent to a polarization $i\omega^{-1}\mathbf{K}$, allowing us to combine the two contributions into a single ‘‘nonclassical’’ polarization term

$$\mathbf{P}^{\text{nc}}(\mathbf{r}) = [\boldsymbol{\pi}(\mathbf{r}) + i\omega^{-1}\mathbf{K}(\mathbf{r})] \delta_{\partial\Omega}(\mathbf{r}). \quad (\text{S14})$$

Next, we assume a thin vacuum layer sandwiched between two materials with thickness t and volume $\partial\Omega'$ to precisely characterize the interface $\partial\Omega$, that is $\partial\Omega' \in \{\mathbf{r} \in \mathbb{R}^3 \mid \exists \mathbf{r}_{\partial\Omega} \in \partial\Omega \text{ st. } |(\mathbf{r} - \mathbf{r}_{\partial\Omega}) \cdot \hat{\mathbf{n}}| \leq t/2\}$. Associated with an indicator function $\theta_{\partial\Omega'}(\mathbf{r}) = 1$ for $\mathbf{r} \in \mathbf{r}_{\partial\Omega'}$ and $\theta_{\partial\Omega'}(\mathbf{r}) = 0$ elsewhere, the layer is related to the interface represented by a surface delta function,

$$\delta_{\mathbf{r}_{\partial\Omega}}(\mathbf{r}) \equiv \lim_{t \rightarrow 0^+} t^{-1} \theta_{\partial\Omega'}(\mathbf{r}). \quad (\text{S15})$$

Thus the nonclassical polarization inside the layer is

$$\mathbf{P}(\mathbf{r} \in \partial\Omega') = [\boldsymbol{\pi} + i\omega^{-1}\mathbf{K}(\mathbf{r})] / t. \quad (\text{S16})$$

For the points outside this region, the polarization is simply the classical one, $\mathbf{P}(\mathbf{r} \in \mathbb{R}^3 \setminus \partial\Omega') = \varepsilon_0 \chi^c(\mathbf{r}) \mathbf{E}(\mathbf{r})$, where χ^c is the classical susceptibility.

Now due to the redefinition of $\partial\Omega'$, the notions of the field in/outside have changed to $f^{\pm} = f(\mathbf{r}_{\partial\Omega} \pm \frac{1}{2}t^{\pm}\hat{\mathbf{n}})$. Notice that the d -parameters framework is a leading-order picture. Thus, the process that swapping \mathbf{E} for \mathbf{E}^c and \mathbf{D} for \mathbf{D}^c is second order which is negligible since the classical parts \mathbf{E}^c and \mathbf{D}^c are only the first order of the quantum-corrected fields \mathbf{E} and \mathbf{D} . This will refer to

$$\boldsymbol{\pi}(\mathbf{r}_{\partial\Omega}) = \varepsilon_0 d_{\perp} \hat{\mathbf{n}} \hat{\mathbf{n}}^T \llbracket \mathbf{E}^c \rrbracket, \quad (\text{S17a})$$

$$\mathbf{K}(\mathbf{r}_{\partial\Omega}) = i\omega d_{\parallel} (\hat{\mathbf{I}} - \hat{\mathbf{n}} \hat{\mathbf{n}}^T) \llbracket \mathbf{D}^c \rrbracket. \quad (\text{S17b})$$

We can substitute the fields $\mathbf{E}^{c\pm}$ to the fields at the interface $\partial\Omega$ classically which can be bridged by $\partial\Omega'$. First, the normal \mathbf{D}^c field is continuous, i.e., $D_{\perp}^{c-} = D_{\perp}^c = D_{\perp}^{c+}$. Thus, we have $E_{\perp}^{c\pm} = E_{\perp}^c / \varepsilon^{c\pm}$ with $\varepsilon^{c\pm} \equiv \varepsilon^c(\mathbf{r}_{\partial\Omega} \pm \frac{1}{2}t^{\pm}\hat{\mathbf{n}})$. We can substitute $\hat{\mathbf{n}} \hat{\mathbf{n}}^T \llbracket \mathbf{E}^c \rrbracket$ for $\hat{\mathbf{n}} \hat{\mathbf{n}}^T \llbracket 1/\varepsilon^c \rrbracket \mathbf{E}$ in Eq. (S17a). Next, the tangential fields \mathbf{E}^c is continuous, i.e., $\mathbf{E}_{\parallel}^{c-} = \mathbf{E}_{\parallel}^c = \mathbf{E}_{\parallel}^{c+}$. Recalling the relation $\mathbf{D}_{\parallel}^{c\pm} = \varepsilon_0 \varepsilon^{c\pm} \mathbf{E}_{\parallel}^c$, we substitute $(\hat{\mathbf{I}} - \hat{\mathbf{n}} \hat{\mathbf{n}}^T) \llbracket \mathbf{D}^c \rrbracket$

for $(\hat{\mathbf{I}} - \hat{\mathbf{n}}\hat{\mathbf{n}}^T)_{\varepsilon_0 \ll \varepsilon^c} \mathbf{E}^c$ in Eq. (S17b). Inserting these two relations back in Eq. (S16), and substituting \mathbf{E}^c for the quantum-corrected field \mathbf{E} (neglecting again the second-order error), we find

$$\mathbf{P}(\mathbf{r} \in \partial\Omega') = \varepsilon_0 t^{-1} \left[d_{\perp} \llbracket 1/\varepsilon^c \rrbracket \hat{\mathbf{n}}\hat{\mathbf{n}}^T - d_{\parallel} \llbracket \varepsilon^c \rrbracket (\hat{\mathbf{I}} - \hat{\mathbf{n}}\hat{\mathbf{n}}^T) \right] \mathbf{E}(\mathbf{r}). \quad (\text{S18})$$

Now we can directly identify the nonclassical susceptibility χ^{nc} as

$$\chi^{\text{nc}}(\mathbf{r}) = t^{-1} \left[d_{\perp} \llbracket 1/\varepsilon^c \rrbracket \hat{\mathbf{n}}\hat{\mathbf{n}}^T - d_{\parallel} \llbracket \varepsilon^c \rrbracket (\hat{\mathbf{I}} - \hat{\mathbf{n}}\hat{\mathbf{n}}^T) \right]. \quad (\text{S19})$$

In the $t \rightarrow 0^+$ limit, we can then finally restore the surface delta function to obtain

$$\chi^{\text{nc}}(\mathbf{r}) = \left[d_{\perp} \llbracket 1/\varepsilon^c \rrbracket \hat{\mathbf{n}}\hat{\mathbf{n}}^T - d_{\parallel} \llbracket \varepsilon^c \rrbracket (\hat{\mathbf{I}} - \hat{\mathbf{n}}\hat{\mathbf{n}}^T) \right] \delta_{\partial\Omega}(\mathbf{r}). \quad (\text{S20})$$

Note that the nonclassical susceptibility is anisotropic and remains a local quantity. The classical and nonclassical susceptibilities will not be simultaneously nonzero, since the classical susceptibility $\chi^c(\mathbf{r})$ is nonzero in $\mathbb{R}^3 \setminus \partial\Omega'$ and χ^{nc} is nonzero only in $\partial\Omega'$. Similar to the bulk permittivity, we can determine the constraints of passivity. We focus on the rate of energy absorption (dissipated power) in the nonclassical layer $\partial\Omega'$: $\partial_t u = \frac{1}{2} \text{Re} \int_{\partial\Omega'} d^3\mathbf{r} \mathbf{E}^\dagger \mathbf{J}$. Recalling that $\mathbf{J} = -i\omega\mathbf{P} = -i\omega\varepsilon_0\chi^{\text{nc}}\mathbf{E}$, we get

$$\partial_t u = \frac{\varepsilon_0}{2} \int_{\partial\Omega'} d^3\mathbf{r} \text{Im} \left[\mathbf{E}^\dagger(\mathbf{r}) (\omega\chi^{\text{nc}}) \mathbf{E}(\mathbf{r}) \right], \quad (\text{S21})$$

where there is the possibility that ω is a complex quantity with $\text{Im} \omega > 0$ to ensure causality. This must be zero or positive for any electric field $\mathbf{E}(\mathbf{r})$ at any position inside the layer $\mathbf{r} \in \partial\Omega'$ to ensure a locally dissipative environment. Accordingly, the imaginary part of the operator $\omega\chi^{\text{nc}}$ must be positive-semidefinite, i.e., $\text{Im} \mathbf{f}^\dagger (\omega\chi^{\text{nc}}) \mathbf{f} \geq 0$ for any $\mathbf{f} \in \mathbb{C}^3$. Since χ^{nc} is diagonal, we can finally cast the constraints from passivity as

$$\text{Im} (\omega d_{\perp} \llbracket 1/\varepsilon^c \rrbracket) \geq 0, \quad (\text{S22a})$$

$$\text{Im} (\omega d_{\parallel} \llbracket \varepsilon^c \rrbracket) \leq 0. \quad (\text{S22b})$$

S4. MODEL SENSITIVITY ANALYSIS

We theoretically verify the contribution of d_{\perp} in the quantum Fresnel law to demonstrate that it can be extracted in principle. Considering an arbitrary model, the relative contribution (or weight) of various input parameters can be studied by calculating how sensitive the outputs are to the inputs. The sensitivity indices can be in several forms such as first-order (outputs to a single input), second-order (outputs to two inputs with potential correlation), and total-order (outputs to the total effect of a single input, including the first-order effect, higher-order effect of a single input).

In this section, we provide two methods to identify and determine the valid frequency regimes where the measurement of d_{\perp} can be successful. The first is the comprehensive Sobol' variance-based sensitivity analysis and the second is a simple method using first-order partial differentiation. The former can calculate all kinds of sensitivity indices, whereas the latter only considers the first-order effects.

A. The Sobol' sensitivity analysis

The Sobol' sensitivity analysis is based on the decomposition of the input parameters variance to the variance of output observables, which not only evaluate the sensitivity of individual parameters but also account for the interactions of multiple parameters [S3; S4; S5; S6; S7]. It uses the Monte Carlo method to sample various input parameter combinations. As long as the sample size is large enough (to be ergodic), all potential parameter combinations can be achieved. Based on the combination of all inputs and corresponding outputs, we can statistically calculate their variance, respectively.

The input arguments ε and d_{\perp} are represented as μ , the outputs ν which are the observables Ψ and Δ , and they are related through the quantum Fresnel equations as $\nu = f(\mu)$. The variances of output variables can be decomposed into the variance of inputs,

$$\text{Var}(\nu) = \sum_i V_{\mu_i} + \sum_{i < j} V_{\mu_i \mu_j} + \cdots + V_{\mu_1 \mu_2 \mu_3 \mu_4}, \quad (\text{S23})$$

where $V_{\mu_i} = \text{Var}_{\mu_i}(E_{\mu_{-i}}(v|\mu_i))$, $V_{\mu_i\mu_j} = \text{Var}_{\mu_i\mu_j}(E_{\mu_{-ij}}(v|\mu_i, \mu_j))$, and so on. Var denotes the variance, E is the expectation value, and μ_{-i} denotes the inputs arguments without μ_i . In such a way, one can define the first-order index as

$$s_{\mu_i}^v = \frac{V_{\mu_i}}{\text{Var}(v)}, \quad (\text{S24})$$

which indicates the individual influence of an input μ_i on the output v . The total-effect index, which describes the contribution of an input with its interactions with the output variance taken into account, can be given as

$$S_{\mu_i}^v = \frac{E_{\mu_{-i}}(\text{Var}_{\mu_i}(v|\mu_{-i}))}{\text{Var}(v)}. \quad (\text{S25})$$

In our Sobol' analysis, we generate 40960 samples within a wide parameter space given by $\text{Re}(\varepsilon) \in [-50, 0]$, $\text{Im}(\varepsilon) \in [0, 10]$, $\text{Re}(d_{\perp}) \in [-3, 3]$ nm, and $\text{Im}(d_{\perp}) \in [-3, 3]$ nm. The result of the total-order indices is shown in Fig. 2 and the result of the first-order indices is presented in Fig. S1. The first-order and total indices jointly indicate that it is possible to ellipsometrically measure d -parameters for high frequencies above the Drude frequency regime.

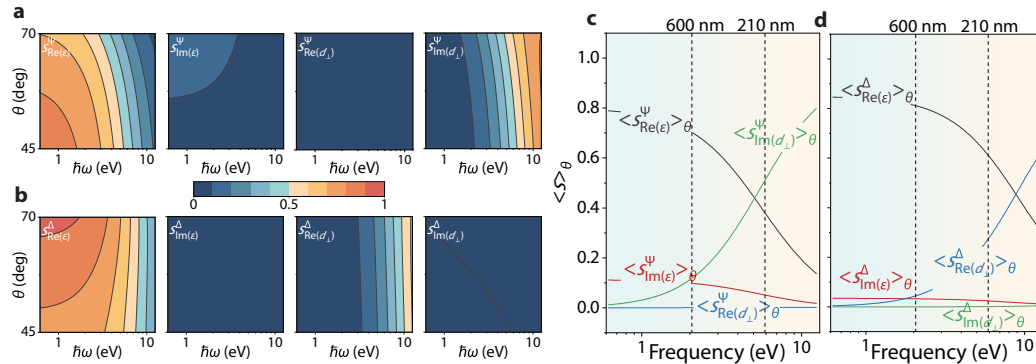


Figure S1. First-order indices of the ellipsometric observables Ψ and Δ a–b. The first-order indices $s_{\varepsilon, d_{\perp}}^{\Psi, \Delta}$ of $\Psi(\theta, \omega)$ (a) and $\Delta(\theta, \omega)$ (b) for input variables $\varepsilon(\omega)$ and $d_{\perp}(\omega)$. **c–d.** Angle-averaged first-order indices $\langle s_{\varepsilon, d_{\perp}}^{\Psi, \Delta} \rangle_{\theta}$. The background color gradient from blue to yellow indicates the increased d_{\perp} contributions towards higher frequencies. The frequency window 2.1–5.9 eV in our experimental analysis is shown by the two vertical dashed lines.

B. The first-order partial differentiation analysis

Complementary to the comprehensive Sobol' analysis, we also use ordinary first-order partial differentiation to evaluate the contributions of various input parameters. We perform the differentiation numerically and the results are shown in Fig. S2. The permittivity ε adopts the tabulated data from Johnson & Christy [S8]. For the differentiation of d_{\perp} , we perform averaging along all differentiation directions on the complex d_{\perp} plane because the evolution direction of d_{\perp} with regard to frequency is unknown (whereas this is known for the bulk permittivity).

The differentiation result shows an abrupt increase of sensitivity to d_{\perp} for frequencies larger than around 2 eV, where the sensitivity to d_{\perp} becomes comparable with that to ε . A representative value of d_{\perp} is chosen as $-1 + 0.5i$ nm in Fig. S2, and we have verified that the differentiation results in Fig. S2 remains similar for other choices of d_{\perp} . This result thus reaches consistency with the Sobol' analysis (Fig. 2 and Fig. S1).

S5. SAMPLE CHARACTERIZATIONS

Our samples are commercially available atomically flat template-stripped Au(111) chips (Platypus Technologies). The thickness of the gold film is ~ 100 nm and can be considered bulk for the frequency regime of interest. We characterized the crystalline structure and the surface roughness of the gold chips.

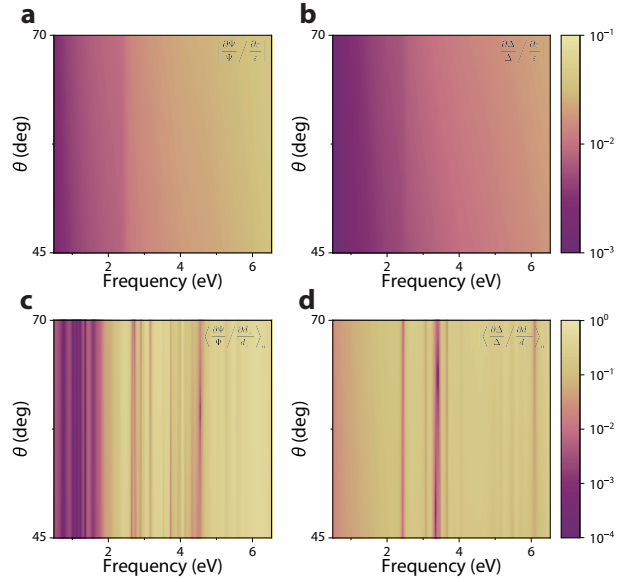


Figure S2. Partial differentiation analysis. **a–b.** Normalized first-order partial differentiation $\left| \frac{\partial \Psi}{\partial \Psi} \frac{\partial \varepsilon}{\partial \varepsilon} \right|$ (a) and $\left| \frac{\partial \Delta}{\partial \Delta} \frac{\partial \varepsilon}{\partial \varepsilon} \right|$ (b). **c–d.** Normalized first-order partial differentiation $\left\langle \left| \frac{\partial \Psi}{\partial \Psi} \frac{\partial d_{\perp}}{\partial d_{\perp}} \right| \right\rangle_{\alpha}$ (c) and $\left\langle \left| \frac{\partial \Delta}{\partial \Delta} \frac{\partial d_{\perp}}{\partial d_{\perp}} \right| \right\rangle_{\alpha}$ (d), where $\langle \rangle_{\alpha}$ denotes the average along all possible differential directions in the complex d_{\perp} plane.

A. Crystalline structure

The crystalline structure of the gold films is dominated by the (111) phase. We confirm it by an X-ray diffraction (XRD) system (Rigaku Miniflex X-ray diffractometer). Figure S3 presents the XRD patterns in the scanning range of $3^{\circ} - 90^{\circ}$. The intense peaks at 38.5° and 82.0° correspond to the (111) and (222) gold orientations, respectively, which confirms the dominance of the Au(111) phase.

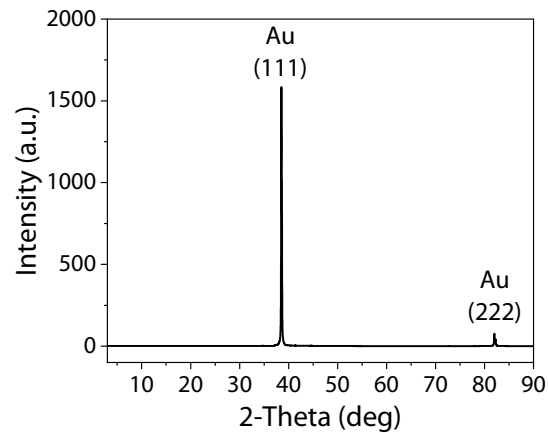


Figure S3. X-ray diffraction analysis of the gold sample. There exist two Bragg peaks corresponding to the (111) and (222) directions with the former peak in dominance.

B. Surface roughness

Figure S4a shows that the idealized flat Au(111) surface, which has an intrinsic roughness on the order of an atom size [S9; S10]. The surface roughness of the gold films is characterized using an atomic force microscope (MFP-3D Infinity AFM). The AFM image of our measured samples is shown in Fig. S4b. The root-mean-square (rms) roughness of the gold films is 0.311 nm.

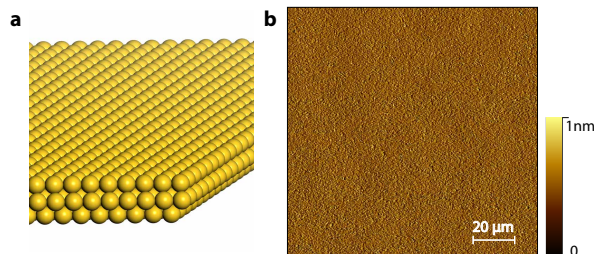


Figure S4. Surface roughness. **a.** Illustration of an idealized atomically flat Au(111) surface. **b.** AFM image of the gold sample. The rms surface roughness is 0.311 nm.

S6. ELLIPSOMETRIC MEASUREMENTS

Spectroscopic ellipsometry is widely used for the precise and non-destructive optical characterization of thin films. It uses linearly polarized light to illuminate samples and detect the polarization-changed signals after interaction with them. The change in polarization state is quantified by two raw measured parameters: amplitude ratio Ψ and phase change Δ , which is related by the reflectance ratio of the complex Fresnel reflection coefficients for p- and s- polarized wave via $r_p/r_s = \tan(\Psi)e^{i\Delta}$ [S11; S12]. In addition, ellipsometry is capable of measuring the reflectance of the p-polarized wave R_p and s-polarized wave R_s of the sample, which can be considered as two additional fitting variables. Importantly, in the modulation and demodulation process of ellipsometry, Ψ and Δ can be obtained from AC signal only, whereas the p- and s- intensity values contain both DC and AC contributions and are thus more vulnerable to external noises (such as the ambient light and $1/f$ noises). Therefore, the incorporation of R_p and R_s will result in increased uncertainty of the fitting [S12]. As a result, only Ψ and Δ are included as observables in our fitting model.

We performed ellipsometric measurements using an RC2 variable-angle spectroscopic ellipsometer. The wavelength range of the measurement spans from $\lambda = 210$ nm to $\lambda = 1690$ nm. The light incident angle of all measurements range from $\theta = 45^\circ$ to $\theta = 70^\circ$ with a step size of 0.2° . The fine angular resolution here is critical for our measurement because it provides sufficient observations for extracting the d_\perp with unprecedented accuracy in previously inaccessible frequency regimes. To validate the consistency of our data, we performed repeated measurements on five gold chips labeled as “Au-1” to “Au-5” at a fixed time interval of 20 min between neighboring measurements.

For the ellipsometric measurement of each sample, measurements were performed within 4 hours after peel-off from the wafer to minimize environmental contamination. The duration of angle scanning of the ellipsometer is 20 min, and each round of measurement was performed consecutively.

Figure S5 shows the standard deviations of the total thirty ellipsometric measurements. The small standard deviations of Ψ and Δ indicate the measurement results are clustered tightly around their mean values (See Fig. 1c and d), which are thus used for extracting the bulk permittivity and d -parameters in Fig. 3b and c.

S7. FITTING METHODOLOGY

A. Weighted nonlinear least-squares fitting

We adopt the nonlinear least-squares method to extract the bulk permittivity and d -parameters simultaneously from the measured Ψ and Δ . We assume the d -parameters are independent of the incident angles

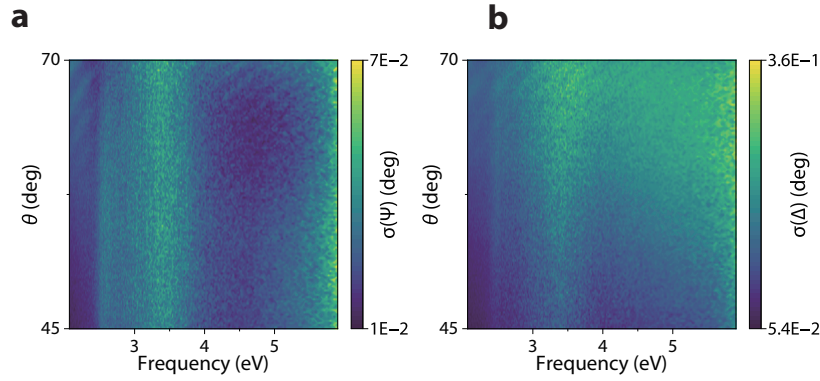


Figure S5. Noise level in ellipsometry observables Ψ and Δ . The standard deviation $\sigma(\Psi)$ and $\sigma(\Delta)$ of all ellipsometric measurements as a function of the incident angle θ and frequency ω .

(i.e., neglecting the nonlocality of d -parameters), and thus the fitting is performed for each frequency at all angles with the loss function L given by

$$L = \sum_i^N \frac{[\Delta_i^{\text{mes}} - \Delta_i^{\text{mod}}]^2}{\sigma_{\Delta,i}^2} + \sum_i^N \frac{[\Psi_i^{\text{mes}} - \Psi_i^{\text{mod}}]^2}{\sigma_{\Psi,i}^2}, \quad (\text{S26})$$

where Δ_i^{mes} and Ψ_i^{mes} are measured observables, Δ_i^{mod} and Ψ_i^{mod} are the model predictions. The summation is over all reflection angles indexed by i , and the residuals are weighted by the standard deviations of the experimental data $\sigma_{\Delta,i}$ and $\sigma_{\Psi,i}$. Because the model is nonlinear, the Levenberg–Marquardt algorithm is used to solve the minimization problem. The confidence intervals are calculated in an iterative way based on the F-test.

In the fitting, we use the Johnson and Christy data of gold [S8] as the initial guess for the bulk permittivity. It is noted that by imposing d -parameters to be zero, the fitting process will produce the classical bulk permittivity as the standard ellipsometry does. The initial value of d_{\perp} is randomly chosen with a magnitude of a few angstroms, and the fitting is repeated for several different initial d_{\perp} to avoid the trapping of the fitting at local optima. We have also assumed $d_{\parallel} = 0$ in the fitting (see discussion and the relaxation of this assumption in Sec. S9).

B. Anterior-measurement Monte Carlo analysis

The previous supplementary section S4 suggests that d_{\perp} can be extracted from the quantum Fresnel equations by ellipsometric means. In the following, we show that d_{\perp} can be obtained through the weighted non-linear least-squares fitting from the measured observables under the experimental noise levels. We follow the spirit of the Monte-Carlo method and ensemble statistics to support the fitting approach. The split-step process is described below.

1. The parameter space is chosen as $\omega \in [2.1, 5.9]$ eV, $\text{Re}(d_{\perp}) \in [-2, 2]$ nm, $\text{Im}(d_{\perp}) \in [-1, 3]$ nm. $\varepsilon(\omega)$ uses the measured dispersive permittivity. The large parameter space ensures that all possible d_{\perp} can be covered. Before conducting the measurement, the ground truths are randomly chosen without being associated with any particular interfaces such that we can show the general utility of the ellipsometric approach.
2. We generate 10^6 ensembles at each noise level, where the parameter combinations are chosen randomly.
3. Each ensemble generates “clean” observables Ψ and Δ at 126 angles from 45° to 70° with a step size of 0.2° , as in the experimental conditions. Then, we add unbiased, normally distributed noise to create the “contaminated” observables at a certain noise level. To better mimic the experimental conditions, the standard deviations of Ψ and Δ are correlated—the former is fixed at a quarter

of the latter, which is consistent with their respective value ranges, i.e., $\psi \in [24.9, 45.0]$ deg and $\Delta \in [70.5, 173.5]$. This is supported by the experimental conditions (Fig. S5) where the noise level of Ψ varies from 0.012° to 0.074° while that of Δ from 0.054° to 0.36° , forming an approximate factor of four difference (Fig. 2e).

4. We apply the weighted non-linear least-square method to extract the bulk permittivity and d_\perp simultaneously from the observables. Then, we analyze the errors between the ground truths and the fitted values across the 10^6 ensembles, which is shown in Fig. 2g–h in the main text.
5. We generate another 10^4 ensembles at each points in Fig. 2f. In that particular calculation, the assumed correlation between $\sigma(\Psi)$ and $\sigma(\Delta)$ is relaxed, and the rest of the steps remain unchanged.

C. Posterior-measurement Monte Carlo analysis

The repeated measurements across samples and separated time (see Supp. Sec. S8) enlarge the database and enable the reduction of fitting errors. We perform additional post-measurement Monte Carlo analysis, where the ground truths are chosen to be the experimentally extracted bulk permittivities and d -parameters (Fig. 3). By doing so, we aim to obtain more comprehensive noise features in our measurement and fitting.

The major goal here is to choose between two fitting strategies:

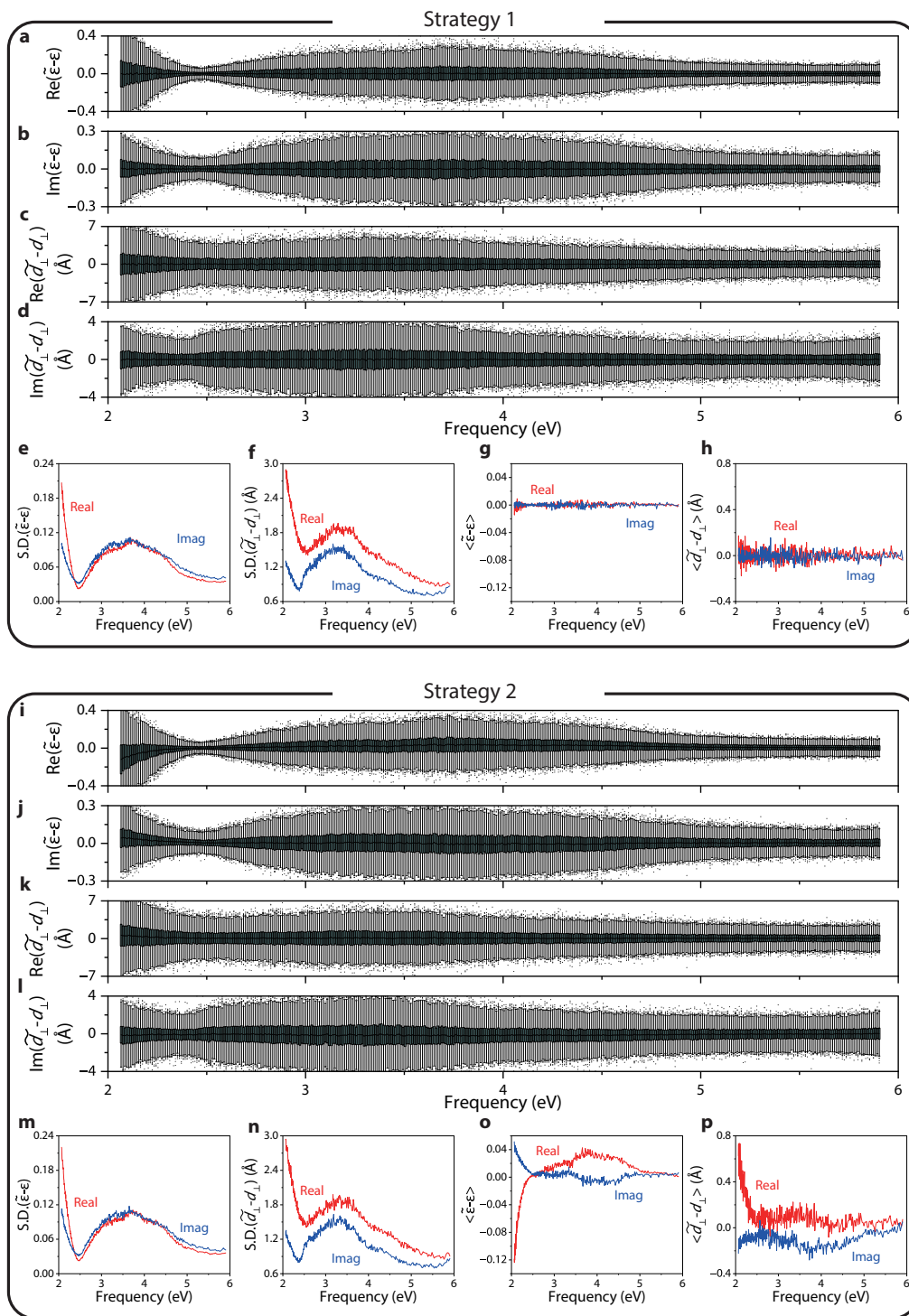
1. Strategy 1 is to first take arithmetic mean of repeated observables and then perform the fitting.
2. Strategy 2 is to perform the fitting first using each set of individual observables and then take the arithmetic mean on the fitted results.

The two strategies are equivalent for linear fittings but may differ for nonlinear ones, which is the case of the quantum Fresnel equation [Eq. (2)]. Analogous to Supp. Sec. S7.B, we utilize the Monte-Carlo method to compare the performance of two strategies based on the following steps.

- We adopt the dispersive measured results obtained in Fig. 3 as the ground truth. For each frequency, we generate 10^3 ensembles and each ensemble contains 30 samples as in our experiment (see Supp. Sec. S8.B).
- Each sample generates “clean” observables Ψ and Δ at 126 angles from 45° to 70° with a step size of 0.2° , matching experimental conditions. Then, we add unbiased noises to create the “contaminated” observables in which the noises are normally distributed, obeying the statistics in Fig. S5 at each angle for each frequency.
- For both strategies, we apply the weighted non-linear least-square method (Supp. Sec. S7.A) to extract the bulk permittivity and d_\perp simultaneously from the observables. For Strategy 1, we generate 30 samples (the same as the number of repeated measurements in our experiment), average them, and perform the fitting with the averaged samples to generate the result within each ensemble. For Strategy 2, we also generate 10^3 ensembles (30 samples within each), perform the fitting individually, and perform statistics to evaluate the arithmetic mean and errors within each ensemble.

The comparison between the two strategies is shown in Fig. S6, where the top box corresponds to Strategy 1 and the bottom box to Strategy 2. Fig. S6a–d and i–l show the box plots of the errors (estimates subtracted by ground truths) in the Monte Carlo simulations. Notably, the uncertainty is minimal in the frequency regime where the Bennett mode appears (see the “waist” of uncertainty near 2.5 eV), which is consistent with the most pronounced residual reduction in Fig. 3a. Fig S6e, f, m, and n show that the uncertainty of the two strategies are comparable. It is worth noting that the standard deviation here refers to that of the mean of 30 samples in each ensemble (such that they are directly comparable to the fitting uncertainty Fig. 3b and c), whereas that in Fig. 2 refer to the standard deviation of a single measurement. Consequently, the former is smaller and the two types of standard deviations are related to each other by a factor of \sqrt{N} , where $N = 30$ is the number of repeated measurements.

Fig. S6g, h, o, and p compare the average errors (without taking absolute values) of the two strategies. Importantly, Strategy 1 is unbiased (Fig. S6g and h); however, Strategy 2 produces biased estimates (Fig. S6o and p) despite the noise added containing zero bias. As a result, we adopt Strategy 1 in our experimental data processing: we take the average of Ψ and Δ (Fig. 1c and d) in the 30 experimental measurements (Supp. Sec. S8) first and then perform the fitting to extract ε and d_\perp simultaneously.



For completeness, we also plot the posterior Monte Carlo estimates without subtracting the ground truth in Fig. S7a and b for direct comparison with the experimental fitting in Fig. 3b and c. Although the experimental confidence intervals are slightly smaller in magnitude (which may be due to cross-measurement correlations in the experiment), the general lineshapes of the Monte Carlo frequency-dependent uncertainty (Fig. S7c and e) are accordant with those of the experimental confidence intervals (Fig. S7d and f).

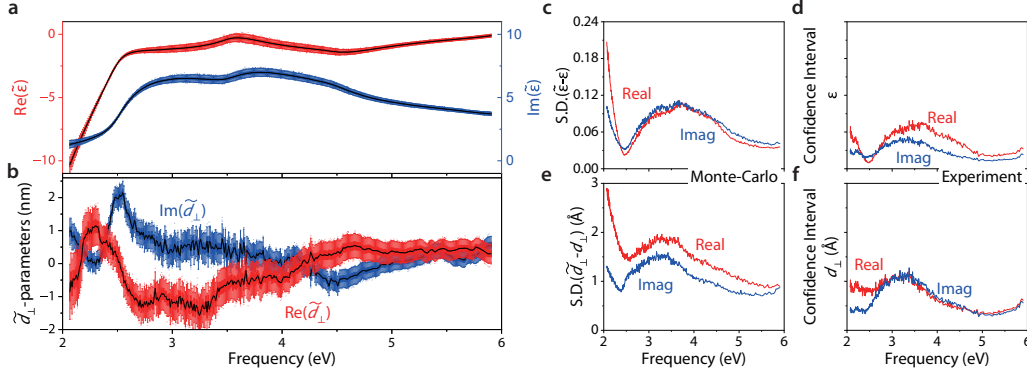


Figure S7. Comparison between posterior Monte-Carlo simulations with experimental data. **a.** Box plot of real (red) and imaginary (blue) parts of Monte Carlo estimates $\tilde{\epsilon}$. **b.** Box plot of real (red) and imaginary (blue) parts of Monte Carlo estimates \tilde{d}_\perp . Black lines indicate the mean values, boxes are the standard deviation $\pm 1\sigma$, whiskers denote the data in the range of $\pm 3\sigma$, and the discrete points are the outliers. **c–d.** Monte Carlo standard deviations of ϵ (c) and experimental fitting confidence interval of ϵ (d), both corresponding to 1σ . **e–f.** Same as c and d but for d_\perp .

Taken together, Secs. S7.A, S7.B, and S7.C jointly confirm the feasibility of extracting bulk permittivities and d -parameters using angle-resolved ellipsometry and judiciously designed fitting strategy.

S8. TEMPORAL AND CROSS-SAMPLE CONSISTENCY

A. Temporal consistency

To investigate the temporal consistency of our measurement, we compared the cross-sample averaged ellipsometric results at all time points (i.e., T_1 to T_6) separated by a fixed time interval of 20 minutes between adjacent measurements. The fitting results from T_1 to T_6 exhibit a high level of consistency, as shown in Fig. S8.

B. Cross-sample consistency

Next, we average the ellipsometric measurement results for each sample at different time points to study the consistency among samples Au-1 to Au-5. Figure S9 presents the time average fitting results of ϵ and d_\perp for the five gold samples, which again exhibit high consistency. Overall, the fitting results confirm the cross-sample stability of the material properties in our measurements.

Jointly shown in Figs. S8 and S9, the consistency of our data across different samples and measurement times indicates the robustness and stability of our experiment and samples. Such consistency also justifies the use of the entire dataset for data analysis.

S9. ALTERNATIVE FITTING ON $d_\perp - d_\parallel$

In the fitting process described in the main text, we adopt the assumption $d_\parallel = 0$ that is generally expected for charge-neutral interfaces. However, such assumption may be violated at some frequencies under specific crystalline structures like the (111) noble-metal surfaces (as in our case) due to the potential contributions from the Shockley surface states [S13; S14].

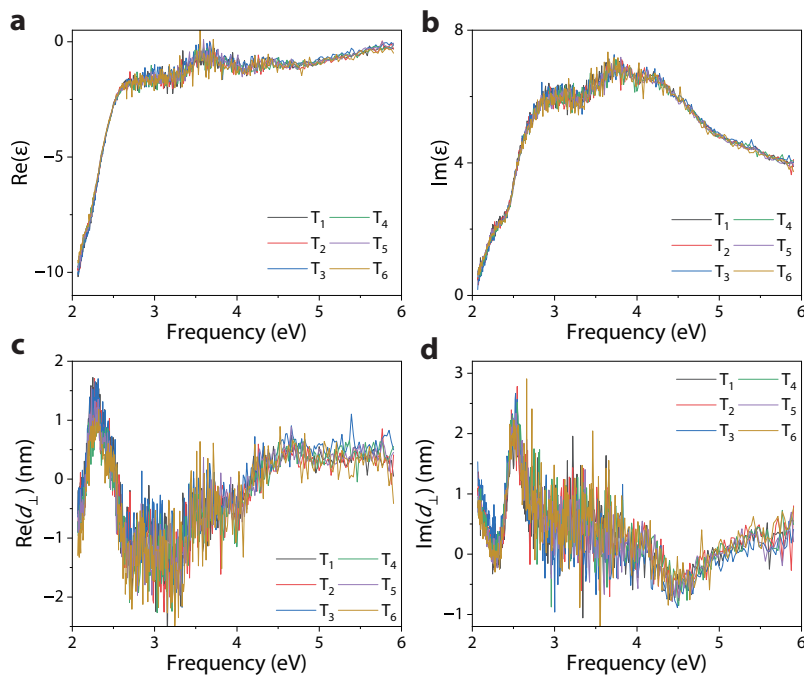


Figure S8. Temporal consistency in the measured permittivity and d -parameters. a-d. Extracted $\text{Re} \epsilon(\omega)$ (a), $\text{Im} \epsilon(\omega)$ (b), $\text{Re} d_{\perp}(\omega)$ (c), and $\text{Im} d_{\perp}(\omega)$ (d) at different time points.

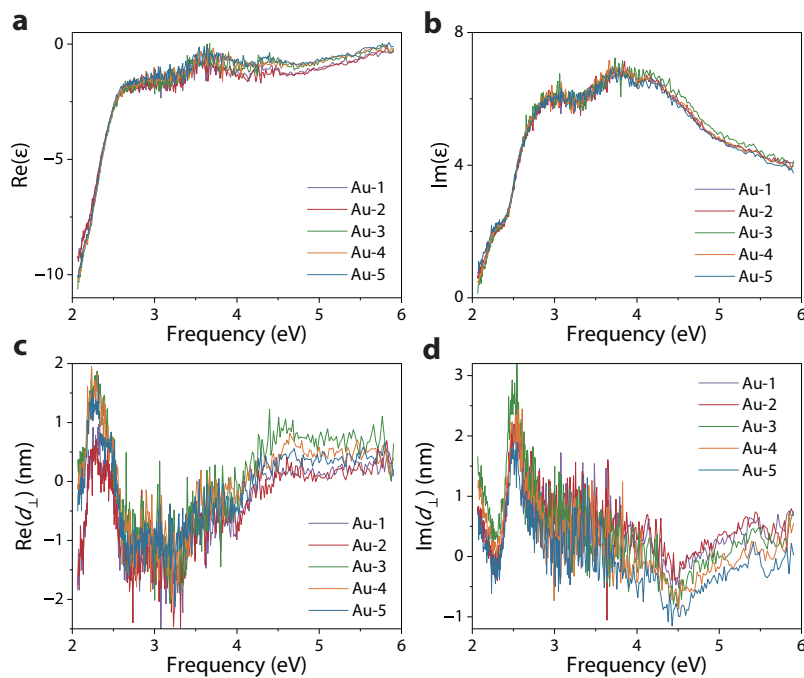


Figure S9. Cross-sample consistency in the measured permittivity and d -parameters. a-d. Extracted $\text{Re} \epsilon(\omega)$ (a), $\text{Im} \epsilon(\omega)$ (b), $\text{Re} d_{\perp}(\omega)$ (c), and $\text{Im} d_{\perp}(\omega)$ (d) from different gold samples.

Bearing this in mind, we perform an alternative fitting on $d_{\perp} - d_{\parallel}$ based on a first-order expansion of the quantum Fresnel law. The ratio of the quantum Fresnel reflection coefficients $\rho = r_p/r_s$ can be expressed as [S15]

$$\rho = \rho^{\text{cl}} \left[1 + 2ik_{z,1} (d_{\perp} - d_{\parallel}) \frac{\varepsilon}{\varepsilon \cot^2 \theta - 1} \right], \quad (\text{S27})$$

where $\rho^{\text{cl}} = r_p^{\text{cl}}/r_s^{\text{cl}}$ is the ratio from classical Fresnel law. We adopt the same fitting method (described in Section S7.A) to this model and obtain the fitted results on $d_{\perp} - d_{\parallel}$ shown in Fig. S10. The fitted $d_{\perp} - d_{\parallel}$ (using Eq. (S27) without assuming $d_{\parallel} = 0$) and d_{\perp} (using Eq. (2) and assuming $d_{\parallel} = 0$) agree with each other quantitatively.

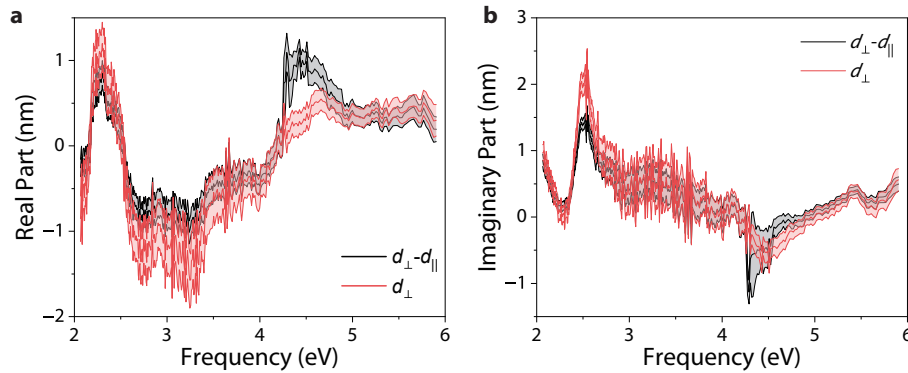


Figure S10. Comparison between fitted d_{\perp} and $d_{\perp} - d_{\parallel}$ with and without assuming $d_{\parallel} = 0$. Shading denotes the confidence interval of 3σ in each fitting.

S10. KRAMERS–KRONIG EXTRAPOLATION

In the Kramers–Kronig relation Eq. (S9), the integration is performed from zero (DC) to infinite frequency. However, practical measurements are always performed under finite frequency windows, which thus requires extrapolation for performing the Kramers–Kronig transformation.

We perform extrapolation in the following manner. First, toward higher frequencies, it has been derived [S2] that $d_{\perp}(\omega) \sim \omega^{-2}$ as $\omega \rightarrow \infty$. We thus impose this condition together with the continuous condition at the high-frequency cutoff. Second, toward DC frequencies below the (screened) plasma frequency, it has been shown that $\text{Re } d_{\perp}$ tends to a constant while $\text{Im } d_{\perp}$ vanishes gradually (see e.g., Ref. S15 and other calculations of d -parameters). Therefore, we impose quadratic decays to -0.4 nm and 0 nm for $\text{Re } d_{\perp}(\omega)$ and $\text{Im } d_{\perp}(\omega)$, respectively, where the asymptotic values are obtained from a previous measurement in the near-infrared regime [S1]. The measurement data and their extrapolation are shown in Fig. S11.

We further note that only KK transformation close to the cut-off of the measurement frequency window will be affected by the particular choice of extrapolation. Within the measurement frequency window, the choice of extrapolation has a very limited impact on the transformation because of the quadratic denominator $\omega'^2 - \omega^2$ in Eq. (S9).

S11. ENERGY DISSIPATION DUE TO THE SURFACE DIPOLE

By virtue of energy conservation, the energy of the incident wave impinging on a planar surface can be divided into three parts: reflection, transmission, and surface dissipation. However, the classical electrodynamic view ignores the surface dissipation term, leading to the well-known energy conservation between reflection and transmission. One can obtain the surface energy dissipation by comparing the classical and quantum Fresnel reflection and transmission coefficients. classically, the energy conservation law is

$$P_{\text{inc}} = P_{\text{ref}} + P_{\text{tra}} = RP_{\text{inc}} + TP_{\text{inc}}, \quad (\text{S28})$$

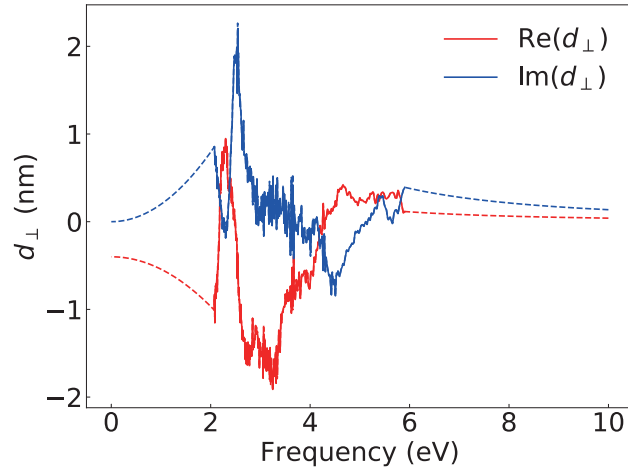


Figure S11. Data used for Kramers–Kronig transformation. Measured data is shown in solid lines, while the extrapolated quadratic decays toward zero and infinite frequencies are shown in dashed lines. The asymptotic limits are 0 nm for $\omega \rightarrow \infty$ and -0.4 nm for $\omega \rightarrow 0$, respectively.

where P_{inc} , P_{ref} , and P_{tra} are the incident, reflected, and transmitted power, respectively, and R and T are power reflection and transmission coefficients, respectively. Evidently, $R + T = 1$.

Taking into account the contribution of d -parameters, there is extra energy dissipation on the surface. The energy conservation law is thus modified as

$$P_{\text{inc}} = P_{\text{ref}}^{\text{nc}} + P_{\text{tra}}^{\text{nc}} + P_{\text{surface}} = R^{\text{nc}} P_{\text{inc}} + T^{\text{nc}} P_{\text{inc}} + \eta P_{\text{inc}}. \quad (\text{S29})$$

where the superscript “nc” stands for “nonclassical”, and the surface energy dissipation ratio is η . Combining Eqs. (S28) and (S29), we can obtain

$$\eta = 1 - R^{\text{nc}} - T^{\text{nc}}. \quad (\text{S30})$$

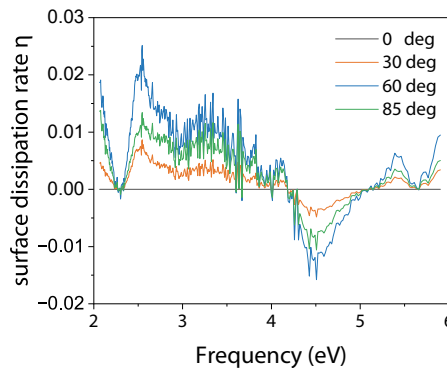


Figure S12. Nonclassical Surface energy dissipation ratio at different incident angles.

Based on Eq. (S30), we apply the measured d -parameters to obtain the surface energy dissipation at different incident angles. At normal incidence, there is no surface dissipation, which increases for larger incident angles, becomes maximal at an intermediate angle, and decreases again for grazing angles. That is because during the increasing of incident angle from 0° to 90° , the impact of d_\perp will first increase with the scaling of $q^2 d_\perp$. With the incident angle approaching 90° , the classical result is restored—transmission vanishes, and reflection tends to unity. The lineshapes of surface dissipation at nonzero and non-90-degree incident angles are qualitatively similar to $\text{Im} d_\perp$. Consistent with the passivity evaluation in Fig. 3d in the main text, the existence of the likely-spurious negative surface dissipation near 4.5 eV is

noticed, which may be due to imperfection in the experimental conditions or underestimated d_{\parallel} contributions (notably, the difference between two fitted results (Fig. S10) with and without assuming $d_{\parallel} = 0$ is also the largest near 4.5 eV, suggesting that there may be considerable d_{\parallel} at those frequencies).

S12. MEASUREMENT LIMITATION

Despite the analytical, experimental, and statistical efforts described above, our measurements still have their limitations. For clarity, completeness, and potential future improvement, we discuss the limitations below:

1. *Surface adsorption contamination.* The samples were measured once peeled from the wafer, and the total measured time was controlled within 4 hours. The measurement time could not be further compressed due to the alignment and angle scanning in each round. During this process under ambient conditions, avoiding undesired surface absorption can be difficult. For example, the adsorbed airborne carbonaceous will decrease the hydrophilicity of the gold surface, thus possibly affecting the measurement [S16; S17; S18]. To mitigate this limitation in the future, it may be possible to perform sample preparation and ellipsometry in vacuum conditions for which products have been developed, e.g., using a VUV-VASE ellipsometer [S19] to isolate the atmosphere from pure dry nitrogen gas thus reduce contamination.
2. *Surface charges.* When the gold samples were peeled from the silicon wafer, there might be charges generated at both surfaces due to friction. These possible charges may invalidate the charge-neutral surface assumption, leading to a nonzero d_{\parallel} .
3. *Surface roughness.* Although our sample is already atomically flat with roughness rms ≈ 0.3 nm, its magnitude is still comparable with the measured d -parameters in certain frequency regimes. It is thus pertinent to advance sample preparation such that the surface roughness can approach the natural crystallinity limit (e.g., for Au(111) the surface roughness should be on the order of 1 Å).

S13. QUANTUM CORRECTIONS TO LOCAL DENSITY OF STATES AND ELECTRON ENERGY LOSS

In this section, we briefly summarize the analytical approaches for calculating the local density of states (LDOS) and electron energy loss with d -parameter contributions taken into account. The additional calculations are shown in Fig. S13, which complement Fig. 4a and b in the main text.

A. LDOS near a planar surface

The local density of states of a point dipole at a distance h away from a $z = 0$ surface (material 1 above and material 2 below, same as the main text convention) can be partitioned into perpendicular and parallel terms as [S20; S21; S22]

$$\frac{\rho_{\perp}(\omega, h)}{\rho_0(\omega)} = 1 + \frac{3}{2} \operatorname{Re} \int_0^{\infty} du \frac{u^3}{\sqrt{1-u^2}} r_p e^{2ik_1 h \sqrt{1-u^2}}, \quad (\text{S31a})$$

$$\frac{\rho_{\parallel}(\omega, h)}{\rho_0(\omega)} = 1 + \frac{3}{4} \operatorname{Re} \int_0^{\infty} du \frac{u}{\sqrt{1-u^2}} [r_s - (1-u^2)r_p] e^{2ik_1 h \sqrt{1-u^2}}, \quad (\text{S31b})$$

where $u = q/k_1$, k_1 is the wavevector in material 1, ρ_0 , ρ_{\perp} , and ρ_{\parallel} denote the original, enhanced perpendicular and parallel LDOS, respectively. Evidently, the nonclassical correction enters via the modified reflection coefficients. For randomly oriented dipoles, the orientation-averaged LDOS is $\langle \rho \rangle = \frac{1}{3}\rho_{\perp} + \frac{2}{3}\rho_{\parallel}$.

B. LDOS near a sphere

The LDOS of a dipole emitter located near a nanosphere is given by [S23; S24]

$$\frac{\rho_{\perp}(\omega, h)}{\rho_0(\omega)} = 1 + \frac{3}{2} \frac{1}{y^2} \sum_{l=1}^{\infty} (2l+1)l(l+1) \operatorname{Re} \left\{ -a_{p,l} \left[h_l^{(1)}(y) \right]^2 \right\}, \quad (\text{S32a})$$

$$\frac{\rho_{\parallel}(\omega, h)}{\rho_0(\omega)} = 1 + \frac{3}{4} \frac{1}{y^2} \sum_{l=1}^{\infty} (2l+1) \operatorname{Re} \left\{ -a_{p,l} \left[\xi_l'(y) \right]^2 - a_{s,l} \left[\xi_l(y) \right]^2 \right\}, \quad (\text{S32b})$$

where $\rho_{\perp}(\omega, h)$ and $\rho_{\parallel}(\omega, h)$ correspond to the LDOS extracted from vertically and horizontally oriented (with regard to the closest spherical surface) dipoles, respectively, $y = k_1(R+h)$, $\xi_l(x) = xh_l^{(1)}(x)$, and $h_l^{(1)}$ is the spherical Hankel function of the first kind. l is a positive integer. The prime superscript notation denotes the differentiation with respect to the arguments inside the parenthesis. $a_{p,l}$ and $a_{s,l}$ are the nonclassical Mie coefficients incorporating d -parameters [S22]

$$a_{p,l} = \frac{\varepsilon_2 j_l(x_2) \Psi_l'(x_1) - \varepsilon_1 j_l(x_1) \Psi_l'(x_2) + (\varepsilon_2 - \varepsilon_1) \left\{ j_l(x_1) j_l(x_2) [l(l+1)] d_{\perp} + \Psi_l'(x_1) \Psi_l'(x_2) d_{\parallel} \right\} R^{-1}}{\varepsilon_2 j_l(x_2) \xi_l'(x_1) - \varepsilon_1 h_l^{(1)}(x_1) \Psi_l'(x_2) + (\varepsilon_2 - \varepsilon_1) \left\{ h_l^{(1)}(x_1) j_l(x_2) [l(l+1)] d_{\perp} + \xi_l'(x_1) \Psi_l'(x_2) d_{\parallel} \right\} R^{-1}}, \quad (\text{S33a})$$

$$a_{s,l} = \frac{j_l(x_2) \Psi_l'(x_1) - j_l(x_1) \Psi_l'(x_2) + (x_2^2 - x_1^2) j_l(x_1) j_l(x_2) d_{\parallel} R^{-1}}{j_l(x_2) \xi_l'(x_1) - h_l^{(1)}(x_1) \Psi_l'(x_2) + (x_2^2 - x_1^2) h_l^{(1)}(x_1) j_l(x_2) d_{\parallel} R^{-1}}, \quad (\text{S33b})$$

where $x_j = k_j R$, $j \in \{1, 2\}$, $\Psi_l(x) = x j_l(x)$, and j_l is the spherical Bessel function of the first kind.

First, we examine the average LDOS of a randomly oriented dipole emitter near a gold sphere [S22; S24; S25] close to the dipolar localized surface plasmon resonance in Fig. 4a (Supp. Sec. S13.B), where on-resonance LDOS is further boosted with quantum corrections taken into account. Also incidentally, detuned from the dipolar resonance towards small frequencies around 2.1 eV, the classical reduction of LDOS is notably plateaued by the Landau damping.

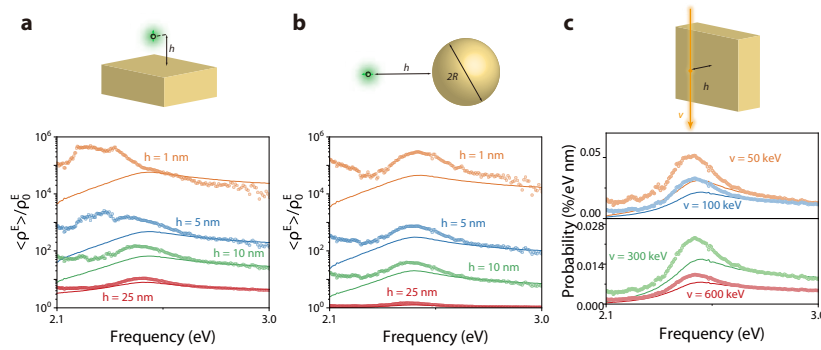


Figure S13. Quantum corrections to the local density of states and electron energy loss. **a.** LDOS near a planar gold surface at different separations h . **b.** LDOS at a different separation of h from a gold sphere with a fixed radius $R = 5$ nm. **c.** Electron energy loss of different velocities above a fixed separation of $h = 5$ nm above a planar gold surface. Classical and nonclassical calculations are denoted by solid lines and dots, respectively. We use the measured bulk permittivities and d -parameters for the calculations.

C. Free electron energy loss near a planar surface

Assuming the surface at $z = 0$ and the velocity of the electron is $\mathbf{v} = v\hat{\mathbf{x}}$ with distance h above the surface, the electron energy loss probability per unit length is

$$\frac{d\Gamma(\omega)}{dx} = \frac{2\alpha}{\pi c \beta^2} \int_0^{\infty} \frac{dk_y}{q^2} \operatorname{Re} \left\{ e^{i2k_{z,1}h} \left[\frac{k_y^2 \beta^2}{k_{z,1}} r_s - \frac{k_{z,1}}{\varepsilon_1} r_p \right] \right\}, \quad (\text{S34})$$

where $\beta = v/c$, $\alpha \approx 1/137$ is the fine-structure constant, and $k_y = \sqrt{q^2 - (\omega/v)^2}$. Again, modified reflection coefficients contain the nonclassical contributions described by d -parameters [S26]. As Fig. S13c shows, the smaller the velocity of the free electrons, the larger the nonclassical enhancement. This is because electrons of smaller velocity couple to large momenta q , where the d_{\perp} contribution scales as $q^2 d_{\perp}$.

D. Free electron energy loss and cathodoluminescence near a sphere

We propose another way to experimentally probe the Bennett mode by using high-resolution electron energy loss spectroscopy. Consider a point electron beam passing near a gold sphere, the corresponding electron energy loss and cathodoluminescence (CL) can be derived based on the Mie theory [S26; S27; S28]. The EELS and CL probabilities are given by

$$\Gamma_{\text{EELS}}(\omega) = \frac{\alpha}{\omega \sqrt{\epsilon_d}} \sum_{l=1}^{\infty} \sum_{m=-l}^l K_m^2 \left(\frac{\omega(R+h)}{v\gamma_{\epsilon_d}} \right) \times \left[C_{lm}^p(\beta_{\epsilon_d}) \text{Im}\{a_{p,l}\} + C_{lm}^s(\beta_{\epsilon_d}) \text{Im}\{a_{s,l}\} \right], \quad (\text{S35})$$

$$\Gamma_{\text{CL}}(\omega) = \frac{\alpha}{\omega \sqrt{\epsilon_d}} \sum_{l=1}^{\infty} \sum_{m=-l}^l K_m^2 \left(\frac{\omega(R+h)}{v\gamma_{\epsilon_d}} \right) \times \left[C_{lm}^p(\beta_{\epsilon_d}) |a_{p,l}|^2 + C_{lm}^s(\beta_{\epsilon_d}) |a_{s,l}|^2 \right], \quad (\text{S36})$$

where K_m is the modified Bessel function of the second kind, $\beta_{\epsilon_d} = \sqrt{\epsilon_d}v/c$, and the Lorentz factor $\gamma_{\epsilon_d} = (1 - \beta_{\epsilon_d}^2)^{-1/2}$. C_{lm}^p and C_{lm}^s only relate to the electron beam energy (see Ref.[S29] for explicit expressions). The quantum correction enters via the Mie coefficients $a_{p,l}$ and $a_{s,l}$ whose explicit forms are Eq.(S33). Our predictions are shown in Fig. 4b in the main text. The peaks in the quantum corrections exhibit blueshift compared with the classical results. Two peaks emerge in the EELS spectra, with the Bennett mode on the low-frequency side.

S14. FIELD EMISSION MEDIATED BY QUANTUM SURFACE RESPONSE

Here we make new predictions on how field emission could be enhanced by quantum surface response. The principle of field emission is widely used in many applications, especially electron guns in modern electron microscopes. Field emission strongly depends on the work function, which is the difference between the energy level infinitely far in the contacted material (usually assumed vacuum) and the Fermi level of electrons in solids. Here, we show that quantum surface responses driven by external incident light can modify the work function, leading to enhanced or suppressed emission depending on whether $\text{Re } d_{\perp}$ is positive or negative.

The derivation is divided into two parts. We first explain how the d -parameter-mediated field discontinuity modifies the work function, which is then inserted into the Fowler–Nordheim framework to calculate the field emission current.

A. Work function changes with the strong electric field

In the context of d -parameters, nonclassical surface dipoles $\boldsymbol{\pi}$ appears under field excitation via Eq. (S13a) which we may re-express as

$$\boldsymbol{\pi}(\mathbf{r}_{\partial\Omega}) \equiv \epsilon_0 d_{\perp} \llbracket E_{\perp} \rrbracket \hat{\mathbf{n}}, \quad (\text{S37})$$

It is well-established that out-of-plane surface dipoles can form a polarization barrier, thereby changing the work function [S30; S31; S32; S33]. Specifically, the work function change $\Delta\phi = \phi - \phi_0$ (where ϕ_0 is the work function without external fields) due to a surface dipole density is [S34; S35; S36; S37]

$$\Delta\phi = -\frac{e}{\epsilon_0} \pi, \quad (\text{S38})$$

where π denotes the dipole density along the out-of-plane direction for simplified notation.

More concretely, let us consider a TM incident Gaussian pulse onto an equivalent infinitesimal planar metallic surface (surface normal direction being z). The amplitude of the total field along z is

$$E_{\perp}^{+} = F_0 \sin \theta \left(e^{-ik_{z,1}z} + r_p e^{ik_{z,1}z} \right) e^{i(qx-\omega t)} e^{-t^2/4\sigma^2}. \quad (\text{S39})$$

Here F_0 is the enhanced peak field, θ is the incident angle, $e^{-t^2/4\sigma^2}$ represents the Gaussian envelope, σ describes the duration of the pulse, $k_{z,1}$ is the out-of-plane wavevector, and q is the in-plane wavevector. Recalling Eq. (S1a) and again assuming $d_{\parallel} = 0$, we have

$$\llbracket D_{\perp} \rrbracket = D_{\perp}^{+} - D_{\perp}^{-} = \varepsilon^{+} E_{\perp}^{+} - \varepsilon^{-} E_{\perp}^{-} = d_{\parallel} \nabla_{\parallel} \cdot \llbracket \mathbf{D}_{\parallel} \rrbracket = 0. \quad (\text{S40})$$

Thus, the relation between the modified work function and the incident field at the $z = 0$ surface is given by

$$\Delta\phi = -\frac{e}{\varepsilon_0} \text{Re}[\pi] = -\frac{e}{\varepsilon_0} \cdot \text{Re} \left[d_{\perp} \varepsilon_0 \frac{\varepsilon^{-} - \varepsilon^{+}}{\varepsilon^{-}} E_{\perp}^{+} \right] = -eF_0 \text{Re} \left[d_{\perp} \frac{\varepsilon^{-} - \varepsilon^{+}}{\varepsilon^{-}} \sin \theta (1 + r_p) e^{i(qx-\omega t)} e^{-\frac{t^2}{4\sigma^2}} \right]. \quad (\text{S41})$$

For simplicity, we consider the average change of work function within the entire pulse duration:

$$\langle \Delta\phi \rangle = \left\langle -eF_0 \Theta(-F(t)) \text{Re} \left[d_{\perp} \frac{\varepsilon^{-} - \varepsilon^{+}}{\varepsilon^{-}} \sin \theta (1 + r_p) e^{i(qx-\omega t)} e^{-\frac{t^2}{4\sigma^2}} \right] \right\rangle. \quad (\text{S42})$$

Here $\Theta[-F(t)]$ is the Heaviside function to ensure that only half-cycles of $F(t) < 0$ are considered, during which electrons can be pulled outside the material. Therefore, electron spill-out results in a negative surface dipole layer, causing the work function to increase. On the contrary, electron spill-in leads to a positive surface dipole layer and reduction of work function. The averaged change of the work function is shown in Fig. S14a. The resulting Keldysh parameter [S38] from Eq. S42 is on the order of unity, which enables us to model the electron field emission in the Fowler–Nordheim regime.

B. The field emission current

The Fowler–Nordheim model describes the field emission current escaping from the solid surface when a strong field is applied. Here we adopt the Fowler–Nordheim equation in the form of [S39; S40; S41]

$$J_{\text{FN}} = \frac{e^3}{16\pi^2 \hbar} \frac{[F(t)]^2}{\phi} \Theta[-F(t)] e^{\frac{4\sqrt{2m\phi^3}}{3\hbar e F(t)}}, \quad (\text{S43})$$

where $F(t) = \text{Re}(E_{\text{inc}})$ is the incident field. The average current density is [S42]

$$J = f_{\text{R}} \int_{-T_{\text{R}}/2}^{T_{\text{R}}/2} J_{\text{FN}}(t) dt, \quad (\text{S44})$$

where $T_{\text{R}} = 1/f_{\text{R}}$ and f_{R} is the repetition rate. Figure S14b shows that the current enhancement or suppression depends strongly on $\text{Re} d_{\perp}$ and incident angles. It is found that $\text{Re} d_{\perp} > 0$ leads to current suppression and $\text{Re} d_{\perp} < 0$ leads to current enhancement.

Moreover, the incident angle also has a large impact on the enhancement because of the balance between two counteractive factors. First, smaller incident angles lead to smaller electric field components (and their discontinuity) along the normal z direction, resulting in weakened modifications (either enhancement or suppression) to field emission. Second, toward larger incident angles close to 90° , $r_p \rightarrow -1$, resulting in a vanishing total field. Jointly the considerations imply an optimal, intermediate incident angle (close to 60° for the case shown in Fig. S14b) that maximizes the nonclassical modifications to field emission.

REFERENCES

* Z. C., S. Y., and Z. X. contributed equally to this work.

† yyg@hku.hk

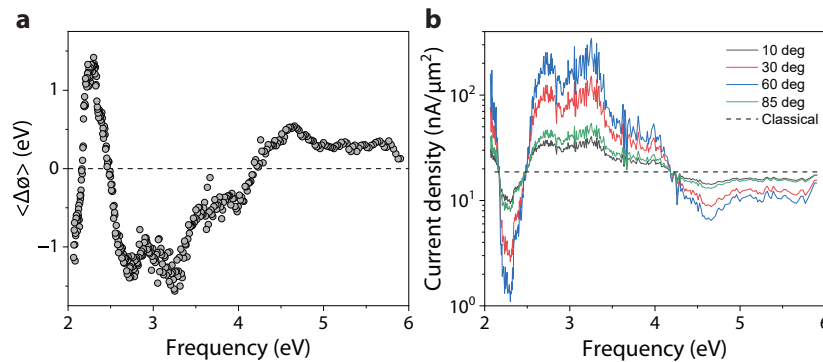


Figure S14. Modified work function under quantum surface corrections and the resulting field emission current density. **a.** Modified work function under pulsed laser pump at different center frequencies. Here the original work function is chosen as $\phi_0 = 5.1$ eV, the peak field is 15 V/nm, the repetition rate $f_R = 100$ MHz and the full-width at half-maximum duration is 10 fs which contains enough number of optical cycles such that the phase of the pulse plays a negligible role here. **b.** Predicted field emission current density under various incident angles.

- [S1] Y. Yang, D. Zhu, W. Yan, A. Agarwal, M. Zheng, J. D. Joannopoulos, P. Lalanne, T. Christensen, K. K. Berggren, and M. Soljačić, *Nature* **576**, 248 (2019).
- [S2] B. Persson and P. Apell, *Physical Review B* **27**, 6058 (1983).
- [S3] I. M. Sobol', *Mathematics and Computers in Simulation* **55**, 271 (2001).
- [S4] A. Saltelli, *Computer Physics Communications* **145**, 280 (2002).
- [S5] A. Saltelli, P. Annoni, I. Azzini, F. Campolongo, M. Ratto, and S. Tarantola, *Computer Physics Communications* **181**, 259 (2010).
- [S6] T. Iwanaga, W. Usher, and J. Herman, *Socio-Environmental Systems Modelling* **4**, 18155 (2022).
- [S7] J. Herman and W. Usher, *The Journal of Open Source Software* **2** (2017).
- [S8] P. B. Johnson and R.-W. Christy, *Physical Review B* **6**, 4370 (1972).
- [S9] J. Yu and Y. Namba, *Applied physics letters* **73**, 3607 (1998).
- [S10] Y. Namba, J. Yu, J. M. Bennett, and K. Yamashita, *Applied Optics* **39**, 2705 (2000).
- [S11] H. Tompkins and E. A. Irene, *Handbook of Ellipsometry* (William Andrew, 2005).
- [S12] H. Fujiwara, *Spectroscopic Ellipsometry: Principles and Applications* (John Wiley & Sons, 2007).
- [S13] P. J. Feibelman, *Progress in Surface Science* **12**, 287 (1982).
- [S14] A. R. Echarri, P. A. D. Gonçalves, C. Tserkezis, F. J. García de Abajo, N. A. Mortensen, and J. D. Cox, *Optica* **8**, 710 (2021).
- [S15] A. Liebsch, *Electronic Excitations at Metal Surfaces* (Springer Science & Business Media, 2013).
- [S16] R. L. Olmon, B. Slovick, T. W. Johnson, D. Shelton, S.-H. Oh, G. D. Boreman, and M. B. Raschke, *Physical Review B* **86**, 235147 (2012).
- [S17] S. Lee and R. Staehle, *Corrosion* **52** (1996).
- [S18] L. Chai and J. Klein, *Langmuir* **23**, 7777 (2007).
- [S19] J. N. Hilfiker, B. Singh, R. A. Synowicki, and C. L. Bungay, in *Metrology, Inspection, and Process Control for Microlithography XIV*, Vol. 3998 (SPIE, 2000) pp. 390–398.
- [S20] L. Novotny and B. Hecht, *Principles of Nano-optics* (Cambridge University Press, 2012).
- [S21] R. Carminati, A. Cazé, D. Cao, F. Peragut, V. Krachmalnicoff, R. Pierrat, and Y. De Wilde, *Surface Science Reports* **70**, 1 (2015).
- [S22] P. A. D. Gonçalves, T. Christensen, N. Rivera, A.-P. Jauho, N. A. Mortensen, and M. Soljačić, *Nature Communications* **11**, 366 (2020).
- [S23] H. Chew, *The Journal of Chemical Physics* **87**, 1355 (1987).
- [S24] T. Christensen, W. Yan, S. Raza, A.-P. Jauho, N. A. Mortensen, and M. Wubs, *ACS Nano* **8**, 1745 (2014).
- [S25] M. H. Eriksen, C. Tserkezis, N. A. Mortensen, and J. D. Cox, *Nanophotonics* (2024).
- [S26] P. A. D. Gonçalves and F. J. García de Abajo, *Nano Letters* **23**, 4242 (2023).
- [S27] F. J. García de Abajo and A. Howie, *Physical review letters* **80**, 5180 (1998).
- [S28] F. J. García de Abajo, *Physical Review B* **59**, 3095 (1999).
- [S29] F. J. García de Abajo, *Reviews of modern physics* **82**, 209 (2010).
- [S30] R. Smoluchowski, *Physical Review* **60**, 661 (1941).
- [S31] J. Fleig and J. Jamnik, *Journal of the Electrochemical Society* **152**, E138 (2005).
- [S32] L. Vitali, G. Levita, R. Ohmann, A. Comisso, A. De Vita, and K. Kern, *Nature Materials* **9**, 320 (2010).
- [S33] A. Kahn, *Materials Horizons* **3**, 7 (2016).
- [S34] R. Forbes, *Journal of Physics D: Applied Physics* **11**, L161 (1978).
- [S35] T.-C. Leung, C. Kao, W. Su, Y. Feng, and C. T. Chan, *Physical Review B* **68**, 195408 (2003).
- [S36] H. Ibach, *Physics of Surfaces and Interfaces*, Vol. 12 (Springer, 2006).

- [S37] M. Ávila, M. F. Juárez, and E. Santos, *ChemElectroChem* **7**, 4269 (2020).
- [S38] L. Keldysh, *Soviet Physics JETP* **20**, 1307 (1965).
- [S39] R. H. Fowler and L. Nordheim, *Proceedings of the Royal Society of London. Series A, Containing Papers of a Mathematical and Physical Character* **119**, 173 (1928).
- [S40] P. Keathley, W. Putnam, P. Vasireddy, R. Hobbs, Y. Yang, K. Berggren, and F. Kärtner, *Nature Physics* **15**, 1128 (2019).
- [S41] K. L. Jensen, *Journal of Applied Physics* **135**, 111101 (2024).
- [S42] W. P. Putnam, R. G. Hobbs, P. D. Keathley, K. K. Berggren, and F. X. Kärtner, *Nature Physics* **13**, 335 (2017).